JCTC Journal of Chemical Theory and Computation

Article

Cite This: J. Chem. Theory Comput. 2019, 15, 2780−2796

pubs.acs.org/JCTC

Adaptive Dimensional Decoupling for Compression of Quantum Nuclear Wave Functions and Efficient Potential Energy Surface Representations through Tensor Network Decomposition

Nicole DeGregorio and Srinivasan S. Iyengar*

Department of Chemistry and Department of Physics, Indiana University, 800 E. Kirkwood Ave, Bloomington, Indiana 47405, United States

ABSTRACT: We present an approach to reduce the computational complexity and storage pertaining to quantum nuclear wave functions and potential energy surfaces. The method utilizes tensor networks implemented through sequential singular value decompositions. Two specific forms of tensor networks are considered to adaptively compress the data in multidimensional quantum nuclear wave functions and potential energy surfaces. In one case the well-known matrix product state approximation is used whereas in another case the wave function and potential energy surface space is initially partitioned into "system" and "bath" degrees of freedom through singular value decomposition, following which the individual system and bath tensors (wave functions and potentials) are in turn decomposed as matrix product states. We postulate that this leads to a mean-field version of the well-known projectionally entangled pair state known in the tensor networks community. Both formulations appear as special cases of more general higher order singular value decompositions known in the mathematics literature as Tucker decomposition. The networks are then used to study the hydrogen transfer step in the oxidation of isoprene by peroxy and hydroxy radicals. We find that both networks are extremely efficient in accurately representing quantum nuclear eigenstates and potential energy surfaces and in computing inner products between quantum nuclear eigenstates and a final-state basis to yield product side probabilities. We also present formal protocols that will be useful to perform explicit quantum nuclear dynamics.

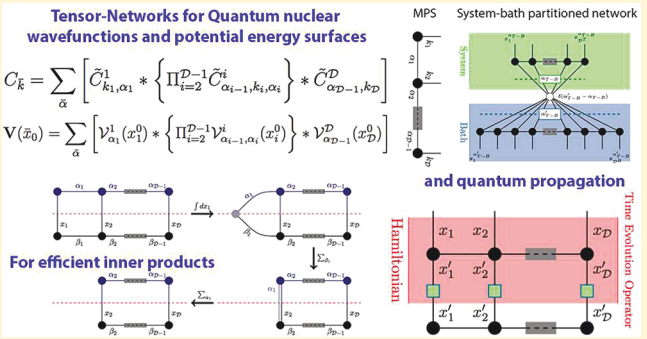

I. INTRODUCTION

Quantum mechanical dynamics is an exponential scaling computational problem.[1−4] This *curse of dimensionality* is illustrated in Figure 1 through two coupled degrees of freedom represented using the red and teal colors. The classical problem (Figure 1a) requires the computation of exactly one force at each instant in time. The quantum mechanical problem (Figure 1b), on the other hand, requires a total of N^2 forces assuming N discretizations along each axis. This is due to the probabilistic distribution of the quantum mechanical degrees of freedom. In other words at every instant in time all of the possible configurational samples along each dimension exert a potential toward every possible realization along the other dimension, thus resulting in a maximum of N^2 computations. In higher dimensions, the classical problem is chaotic[5] and the complexity of the quantum problem grows exponentially with dimensionality of the problem.[1,2]

Despite the implications of the previous paragraph, quantum chemistry and condensed matter physics have flourished due to the adaptive tailoring of correlation and complexity in practical systems as available from (a) atom-centered or plane-wave basis representations for electronic structure and (b) perturbative approximations to correlation. Indeed the discussion on complexity above may be recast in the language of correlation, where it may be stated that, whenever the degrees of freedom represented by the vertical axis in Figure 1 behave differently depending on the location along the horizontal axis, the two dimensions are correlated to at least some extent, and it is this aspect that defines complexity. By extension, when the two degrees of freedom are uncorrelated, the probability (and the wave function) is a product approximation, and the computational complexity reduces drastically. Indeed the success of density matrix renormalization group (DMRG)[6−13] and tensor networks[14,15] in condensed matter physics[16,17] and more recently in quantum chemistry[13,18] arises from the so-called "area-law"[14,19,20] where it is noted that most practical systems only occupy a small portion of the exponentially scaling direct-product space that is available to the fully correlated system.

In this publication we employ tensor-networks to

(a) gauge the degree of compression of correlation or entanglement[21−25] in the quantum mechanical wave function describing reduced-dimensional nuclear degrees of freedom

(b) gauge the associated degree of compression of correlation or entanglement in the Hamiltonian, and specifically the

Received: October 31, 2018
Published: April 19, 2019

DOI: 10.1021/acs.jctc.8b01113
J. Chem. Theory Comput. 2019, 15, 2780−2796

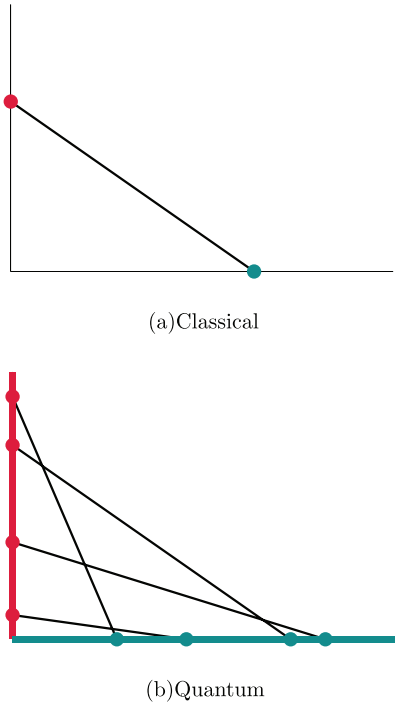

Figure 1. Two degrees of freedom, represented using colors red and teal, are treated classically in part a and quantum-mechanically in part b. In the classical regime, one force calculation is required at every instant in time, and this is represented in part a using the black solid line joining the red and teal circles. The quantum analogue allows both red and teal degrees of freedom to be delocalized, which is represented as red and teal lines in part b. This then requires that the number of potential calculations grow quadratically and a few such interactions are shown using solid lines in part b. When a third degree of freedom is included the quantum mechanical picture grows with cubic complexity and, in general, in $\mathcal{D}$-dimensions, as $O(N^{\mathcal{D}})$, thus yielding the exponential scaling behavior of quantum mechanical computation.

potential energy surface that plays a critical role in quantum nuclear propagation and eigenstate evaluation

(c) use a and b to provide rationales for the associated degree of compression involved in the action (propagation and diagonalization) of operators on the wave function as a step toward the reduction in scaling of quantum dynamical problems for nuclear degrees of freedom.

We introduce a robust computational scheme to reduce the complexity involved in storage, propagation, and diagonalization of general multiconfigurational wave functions. The method uses sequential singular value decompositions[23,26−31] to compress multidimensional, multiconfigurational states. We draw parallels to digital signal processing where time-series of images are compressed using similar numerical schemes and in that case utilized to analyze complex time evolving digital data. We do the same here by probing complex hydrogen transfer reactions that involve critical quantum nuclear effects by using tensor networks to represent the quantum nuclear wave function and potential surface.

The paper is organized as follows: In section II we introduce two different kinds of tensor networks that we utilize to reduce the complexity of multiconfigurational nuclear wave functions. The specific problem we study using these ideas is the Leuven isoprene mechanism,[32−40] introduced in section III. This mechanism provides an explanation for the higher than expected $HO^{\bullet}$ radical concentrations observed[32−40] in rainforest regions. Here isoprene (a volatile organic compound[32,38−41]) reacts with O_2 and $HO^{\bullet}$ radical leading to the formation of RO_2 radicals that are then proposed[33−35] to rearrange through an internal hydrogen transfer to allow the recreation of the $HO^{\bullet}$ radical without consumption of NO_X. In ref 42 we showed that this hydrogen transfer process may have significant quantum nuclear effects including tunneling, and in this publication, we make use of the proposed tensor networks to reduce the computational complexity in such problems. Critical features from ref 42, as relevant to the current publication, are described in Appendix A. In section IV we conduct a detailed error analysis and gauge the extent of data compression of the nuclear wavepackets achieved through use of tensor networks. We note that less than 1% of wavepacket data is necessary when adaptive tensor networks are chosen. In section V the tensor network form of the nuclear wave function is used to compute hydrogen-transfer product side probability at much reduced computational cost. It must however be noted that the product side probabilities computed here use the adiabatic approximation, that is the nuclear eigenstates are used to compute the transition probabilities. This is clearly not sufficient to describe the hydrogen transfer reactions, as noted in ref 43, where nonadiabatic effects were included through explicit wavepacket propagation. To achieve this, it is critical to also consider tensor network forms of the Hamiltonian and time-evolution operators to construct explicit propagation. Hence in section V.B, representing the Hamiltonian and the time evolution operator as tensor networks is discussed along with results for representing the potential energy surface in efficient tensor network form. The theoretical rationale that allows efficient propagation and observable calculations is presented in Appendix B. Conclusions are given in section VI.

II. REPRESENTING MULTICONFIGURATIONAL WAVEFUNCTIONS AND OPERATORS ACTING ON THESE FUNCTIONS AS TENSOR NETWORKS

Consider a multiconfigurational wave function in arbitrary dimensions:

$$\Psi(\bar{x}) = \sum_{k_1,k_2,\cdots,k_i,\cdots,k_{\mathcal{D}}} C_{k_1,k_2,\cdots,k_i,\cdots,k_{\mathcal{D}}} \left[\prod_i^{\mathcal{D}} \psi_{i,k_i}(x_i)\right] = \sum_{\bar{k}} C_{\bar{k}} \left[\prod_i^{\mathcal{D}} \psi_{i,k_i}(x_i)\right] \quad (1)$$

Here $\bar{k}$ is a vector index, with components $\bar{k} \equiv \{k_1, k_2, \cdots, k_i, \cdots, k_{\mathcal{D}}\}$ with k_i being the index to a specific basis function along the ith dimension. It is further assumed here that there are N basis functions available along each dimension. Similarly, $\bar{x} \equiv \{x_1, x_2, \cdots, x_i, \cdots, x_{\mathcal{D}}\}$. The quantities $\psi_{i,k_i}(x_i)$ are the k_ith basis function along dimension i and the sum over $\bar{k}$ signifies an independent set of summations over the individual dimensions within $\{k_i\}$. The quantity $C_{\bar{k}}$ constitutes a tensor of rank $\mathcal{D}$, comprising of $N^{\mathcal{D}}$ elements, and we (a) adaptively gauge the correlations captured in this tensor and present a computational scheme that compresses the information in this tensor while maintaining accuracy, (b) inspect the associated correlations of the potential surface (which is also a rank $\mathcal{D}$ tensor as we see below) and similarly compress the potential, and (c) develop a general adaptive scheme for the action of the Hamiltonian (and hence by extension, the time-evolution

DOI: 10.1021/acs.jctc.8b01113
J. Chem. Theory Comput. 2019, 15, 2780−2796

operator) that exploits this reduction and affect the computational scaling in a favorable manner. It is important to note that the terms inside the square brackets, [···], in eq 1, can be any basis; for example, in ref 44 a multiwavelet basis is used to provide a quantum mechanical description of nuclear degrees of freedom. Modifying the basis to control the extent of correlation captured (such as through the use of product basis[45]) is one way to control the computational efficiency. If approximations to delta functions are employed as basis functions, such as the discrete variable representation (DVR)[46,47] or distributed approximating functionals (DAF)[48−52] or other kinds of interpolating functions[44,53,54] arranged on a grid along each dimension, then eq 1 may be written as

$$\Psi(\bar{x}) = \sum_{\bar{x}_0} \Phi(\bar{x}_0)\left[\prod_i \mathcal{A}(x_i - x_i^0)\right] \tag{2}$$

where, as before, $\bar{x}_0 \equiv \{x_1^0, x_2^0, \cdots, x_i^0, \cdots\}$ and $\Phi(\bar{x}_0)$ approaches $\Psi(\bar{x}_0)$, when $\mathcal{A}$ tends to a true delta function. Furthermore, $\Phi(\bar{x}_0)$ may also be thought of as a rank-$\mathcal{D}$ tensor, much like, $C_{\bar{k}}$ in eq 1, since the grid space $\bar{x}_0$ grows exponentially with dimensionality. It is also important to note that in both eqs 1 and 2 the complexity of storage of and operations on both $C_{\bar{k}}$ and $\Phi(\bar{x}_0)$ grow exponentially with dimension. In the applied mathematics and signal processing communities,[55] both, eqs 1 and 2 define the so-called Tucker form.[56] (Please see eq 1 in ref 55 for a concise definition of the Tucker form. Also see the discussion following eq 5 in ref 57.) The corresponding form for a potential surface may be written as

$$\tilde{\mathbf{V}}(\bar{x}) = \sum_{\bar{x}_0} \mathbf{V}(\bar{x}_0)\left[\prod_i \mathcal{A}(x_i - x_i^0)\right] \tag{3}$$

and here again $\mathbf{V}(\bar{x}_0)$ may be thought of as a rank-$\mathcal{D}$ tensor. In the following sections we will construct an adaptive formalism where the coupling between dimensions, evident from the rank-$\mathcal{D}$ tensorial nature of $\mathbf{V}(\bar{x}_0)$, $C_{\bar{k}}$, and $\Phi(\bar{x}_0)$, are gauged automatically using the morphology of tensor networks and the complexity of the coefficients is reduced through tensor network decomposition. In fact, as we discuss below, the complexity of storage for wave functions and potential surfaces and consequently matrix vector operations scales as

$$O[N \times \{N_\alpha \times [2 + (\mathcal{D} - 2) \times N_\alpha]\}] \equiv O[N \times N_{\bar{\alpha}}] \tag{4}$$

where N is the number of grid points in each dimension (equivalent to the number of basis functions in each dimension in the discussion following eq 1), and N_α is an adaptive quantity that captures the correlation between dimensions, as will be discussed later. We find that for the range of *ab initio* potential surfaces considered here $N_\alpha \ll N$ and is independent of N. Furthermore, the quantity, $N_{\bar{\alpha}} \equiv \{N_\alpha \times [2 + (\mathcal{D} - 2) \times N_\alpha]\}$ and is potentially linearly dependent on $\mathcal{D}$ for the potentials and wavepackets considered here. Our approach is based on tensor networks[8,14,58,59] and closely relates to the TT-SOFT[60] and the vDMRG[61] methods, where matrix product states are used to represent the potential, quantum nuclear wave function and the free-propagator in the momentum representation.[60] In ref 60, the potential surface utilized is the one presented in refs 62−64, and in ref 61, the authors employ a local fourth-order Taylor series approximation to the potential. In this paper, we utilize *ab initio* grid-based potential surfaces from ref 42 efficiently created by gauging the local information content in potentials based on the Nyquist-Shannon sampling theorem.[65−67] We demonstrate our implementation for a hydrogen transfer reaction of significance in atmospheric chemistry. Problem specific details can be found in section III and Appendix A.

It is necessary to note connections between the methods described here and the POTFIT method[57,68−71] for potential energy surface representation that is a significant step in improving the computational efficiency for the multilayer form of MCTDH (ML-MCTDH).[72,73] In POTFIT, the potential is expanded as a sum of product[45,57] precisely as in eq 3, with appropriately chosen basis functions[74] represented above as $\{\mathcal{A}(x_i - x_i^0)\}$. But the associated expansion, as noted above and elsewhere[75] retains the exponential scaling complexity of the problem, and the computational prefactor is reduced in POTFIT by choosing the single-particle basis functions in a careful manner;[57] furthermore, reduced scaling options are also available by carefully choosing the off-diagonal elements of $C_{\bar{k}}$ in eq 1 as a product of the relevant diagonal terms,[45] that is $C_{\bar{k}} \equiv \Pi_i C_{k_i}$ in ref 45. Within this context, the POTFIT approach has been further improved through a multilayer representation[75] where dimensions are coupled together in a logical fashion to achieve a tree-like architecture that captures the "local" correlation to reduce the complexity of storage associated with $\mathbf{V}(\bar{x}_0)$ in eq 3.

Here, in addition to using matrix product states[7,8,14,58,59] as approximations to the rank-$\mathcal{D}$ tensors, $\mathbf{V}(\bar{x}_0)$, $C_{\bar{k}}$, and $\Phi(\bar{x}_0)$, we also introduce a second system-bath partitioned tensor network, which adaptively tailors the correlation between the system and bath degrees of freedom involved in the hydrogen transfer problem studied here.

II.A. Tensor Networks Obtained Using Sequential Singular Value Decompositions Allow Tailoring of Entanglement and Correlation to Compress $C_{\bar{k}}$, $\Phi(\bar{x}_0)$, and $\mathbf{V}(\bar{x}_0)$. We employ the machinery of tensor networks[6−8,14] to reduce the complexity of the multiconfigurational coefficients in eqs 1 and 2. Later we also employ these ideas to compress the potential and to reduce the complexity involved in propagation and diagonalization. Tensors networks allow the sequential refinement of a higher rank tensor (such as the coefficients in eqs 1 and 2) into lower rank tensors, that are then linked through internal degrees of freedom, that capture the entanglement or correlation between these lower rank tensors.[14,19−22,59] These internal degrees of freedom are hidden from outside observation or measurement. The size of the space captured within the internal degrees of freedom clearly depicts the complexity, or entanglement entropy,[14,19,20] of a given tensor network and this size is small for most physical systems that obey the so-called area law of entanglement entropy.[14,19,20] Tensor Networks have been used in electronic structure and condensed matter theory through the density matrix renormalization group methodology (DMRG);[7−13] as noted above, recently these have also been used to construct higher order (quartic) approximations to the nuclear vibrational problem[61] and in computing quantum nuclear dynamics trajectories.[60] DMRG utilizes tensor networks to represent properties of correlated systems;[11,13] furthermore, it has been shown that DMRG can provide good approximations to the full CI[9−11] and MCSCF[76−79] wave functions at much reduced computational effort. The form of the DMRG tensor network is that of a matrix product state (MPS).[14] In this publication, we consider MPS but also consider a second network topology that approximates system-bath problems such

DOI: 10.1021/acs.jctc.8b01113
J. Chem. Theory Comput. 2019, 15, 2780−2796

as those encountered in hydrogen transfer reactions described later in this publication. These tensor networks allow the faithful depiction of nuclear wave functions and a suitable illustration for

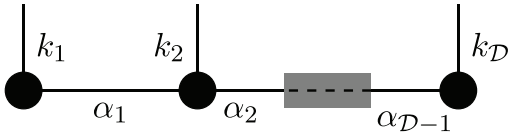

Figure 2. Rank-$\mathcal{D}$ tensor in eq 1 is factorized as per eq 5 which is depicted here. Also see Figure 3

MPS is provided in Figure 2. The MPS state in Figure 2 may be written as

$$C_{\bar{k}} = \sum_{\bar{\alpha}} \left[\tilde{C}^{1}_{k_1,\alpha_1} \times \left\{ \Pi_{i=2}^{\mathcal{D}-1} \tilde{C}^{i}_{\alpha_{i-1},k_i,\alpha_i} \right\} \times \tilde{C}^{\mathcal{D}}_{\alpha_{\mathcal{D}-1},k_{\mathcal{D}}} \right] \tag{5}$$

where the summation vector index $\bar{\alpha} \equiv \{\alpha_1, \alpha_2, \cdots, \alpha_i, \cdots\}$. Equation 5 represents the decomposition of a rank-$\mathcal{D}$ tensor into a set of lower rank tensors where, for example, $\tilde{C}^{1}_{k_1,\alpha_1}$ is a rank-2 tensor, $\tilde{C}^{2}_{\alpha_1,k_2,\alpha_2}$ is a rank-3 tensor, and so on. This decomposition is pictorially represented using Figure 2. Such a decomposition is to be carried out using a sequence of singular value decompositions, and this aspect is also noted in Figure 3 for $\mathcal{D} = 3$. Alternately for the multiconfigurational expansion in eq 2:

$$\Phi(\bar{x}_0) = \sum_{\bar{\alpha}} \left[\chi^{1}_{\alpha_1}(x^0_1) \times \left\{ \Pi_{i=2}^{\mathcal{D}-1} \chi^{i}_{\alpha_{i-1},\alpha_i}(x^0_i) \right\} \times \chi^{\mathcal{D}}_{\alpha_{\mathcal{D}-1}}(x^0_{\mathcal{D}}) \right] \tag{6}$$

where $\{\chi^{i}_{\alpha_{i-1},\alpha_i}(x^0_i)\}$, $\chi^{1}_{\alpha_1}(x^0_1)$, and $\chi^{\mathcal{D}}_{\alpha_{\mathcal{D}-1}}(x^0_{\mathcal{D}})$ are lower dimensional (one-dimensional) functions and hence the method discussed here provides an adaptive decomposition of multidimensional data into lower dimensions. Each node in the tensor network decomposition in Figure 2 represents a lower rank tensor and each line represents an index from the summation sequence $\bar{\alpha}$. For example, the left most node in Figure 2 represents $\tilde{C}^{1}_{k_1,\alpha_1}$ (for eq 5) or $\chi^{1}_{\alpha_1}(x^0_1)$ (for eq 6). Line segments connecting any two nodes are said to "entangle" or "correlate" the reduced dimensional tensors depicted within those nodes. For example, the summation index α_1 in eqs 5 and 6 is (a) an internal index that does not appear on the left side of these equations and (b) connects, correlates, or entangles tensors $\tilde{C}^{1}_{k_1,\alpha_1}$ and $\tilde{C}^{2}_{\alpha_1,k_2,\alpha_2}$ (in eq 5) or $\chi^{1}_{\alpha_1}(x^0_1)$ and $\chi^{2}_{\alpha_1,\alpha_2}(x^0_2)$ in eq 6. While the left-hand sides in eqs 5 and 6 are rank-$\mathcal{D}$ tensors as noted previously, the "correlator-dimension", α_1, picks out dimensions k_1 and introduces rank-2 (for example $\tilde{C}^1$ and Φ^1) and rank-3 (for example C^2 and Ψ^2) tensors. When potential energy surfaces are involved, analogous forms of eq 6 may be written as

$$\mathbf{V}(\bar{x}_0) = \sum_{\bar{\alpha}} \left[\mathcal{V}^{1}_{\alpha_1}(x^0_1) \times \left\{ \Pi_{i=2}^{\mathcal{D}-1} \mathcal{V}^{i}_{\alpha_{i-1},\alpha_i}(x^0_i) \right\} \times \mathcal{V}^{\mathcal{D}}_{\alpha_{\mathcal{D}-1}}(x^0_{\mathcal{D}}) \right] \tag{7}$$

The reduction in complexity in storage of wave function as well as propagation/diagonalization is as follows. If each component of the $\bar{\alpha}$-index vectors only has a modest number of values (which will be adaptively determined using sequential singular value decomposition) the storage and complexity from eqs 5 and 6 reduce to

$$\begin{aligned} & 2 \times N_1 \times N_\alpha + (\mathcal{D}-2) \times [N_1 \times (N_\alpha)^2] \\ &= N_1 \times \{N_\alpha \times [2 + (\mathcal{D}-2) \times N_\alpha]\} \\ &\equiv N_1 \times N_{\bar{\alpha}} \end{aligned} \tag{8}$$

where N_α is the number of values that the intermediate "entanglement" variables (α_1, α_2, etc.) in eqs 5 and 6, can have. For simplicity we have assumed that the number of such values is the same, *i.e.* N_α, for each of these entanglement variables. In addition, we have also introduced $N_{\bar{\alpha}}$ in eq 8, which is equal to the curly bracketed term, $\{\cdots\}$, in the central expression and may be interpreted as the total number of entanglement or internal degrees of freedom in all $\{\alpha_i\}$. In eq 8 we have assumed that N_α is small as compared to N_1. This is consistent with the area law[14,19,20] of entanglement entropy, which is proportional to $N_{\bar{\alpha}}$ and is generally small for most physical problems as compared to $[N_1]^{\mathcal{D}}$. As a result, the complexity depicted in eq 8 scales linearly with N_1 which is the number of basis functions in each dimension, whereas the number of elements in the rank-$\mathcal{D}$ tensors on the left side of eqs 5, 6, and 7 scale exponentially with N_1. The power of the computational method discussed later in this paper, is that we have the flexibility to adaptively gauge the entanglement entropy (through adaptive determination of N_α) for any given situation based on system complexity.

Given that we are specifically targeting quantum nuclear effects in hydrogen transfer reactions here, we have introduced a second kind of tensor network that separates the hydrogen "transfer coordinates" from "bath coordinates" as

$$C_{\bar{k}} = \sum_{\bar{\alpha}_{T-B}} [C^{T}_{\bar{k}_T,\bar{\alpha}_{T-B}} \times C^{B}_{\bar{\alpha}_{T-B},\bar{k}_B}] \tag{9}$$

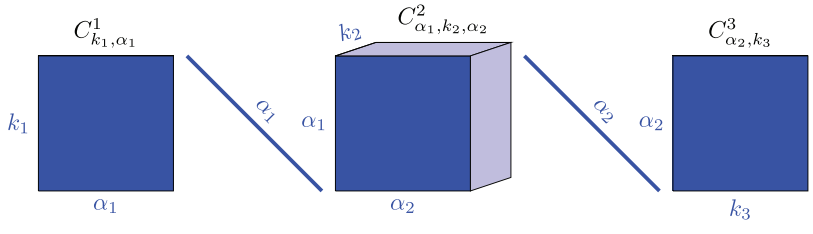

Figure 3. Matrix operations inherently present in a tensor network such as Figure 2. The lower rank tensors are obtained through a sequence of singular value decompositions (SVD). The illustration is provided for a rank-3 tensor, $C_{k1,k2,k3}$, but works identically for rank-$\mathcal{D}$ as noted from Figure 2 and eq 5.

DOI: 10.1021/acs.jctc.8b01113
J. Chem. Theory Comput. 2019, 15, 2780−2796

where $\bar{\alpha}_{T-B}$ are a set of transfer coordinate−bath coordinate correlators, or system-bath entanglement degrees of freedom, that connect the transfer coordinate tensor network, $C^{T}_{\bar{k}_T,\bar{\alpha}_{T-B}}$ with bath tensor network, $C^{B}_{\bar{\alpha}_{T-B},\bar{k}_B}$. An illustration of eq 9 is provided in Figure 4. The individual system and bath tensor

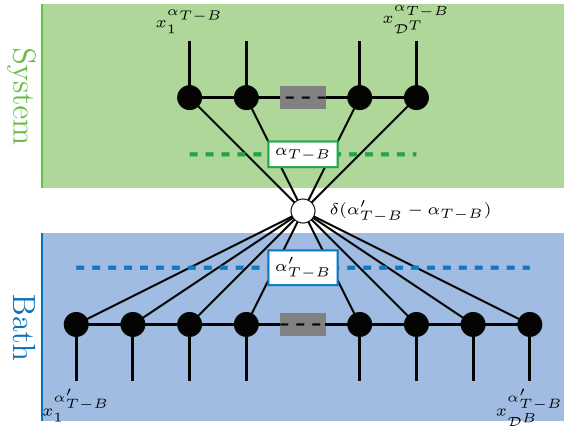

Figure 4. Rank-$\mathcal{D}$ tensor in eq 1 is factorized as per eq 9 and depicted here.

networks can then in turn be written as matrix product states that are now indexed by the correlators, $\bar{\alpha}_{T-B}$, for example

$$C^{T}_{\bar{k}_T,\bar{\alpha}_{T-B}} = \sum_{\bar{\alpha}} \left[\tilde{C}^{1,\bar{\alpha}_{T-B},T}_{k_T^1,\alpha_1} \times \left\{ \Pi_{i=2}^{\mathcal{D}^T-1} \tilde{C}^{i,\bar{\alpha}_{T-B},T}_{\alpha_{i-1},k_T^i,\alpha_i} \right\} \times \tilde{C}^{\mathcal{D}^T,\bar{\alpha}_{T-B},T}_{\alpha_{\mathcal{D}-1},k_T^{\mathcal{D}^T}} \right] \tag{10}$$

and similarly for $C^{B}_{\bar{k}_B,\bar{\alpha}_{T-B}}$. This can be thought of as a "mean-field" version of projected entangled pair state (PEPS).[14,59,80] A PEPS system is a higher dimensional lattice structure of an MPS.[14,59,80] For the system-bath tensor network in Figure 4, one may envision two different matrix product states, namely, the system and the bath states, that are entangled in a "mean-field" fashion as depicted by the white circle in Figure 4. But, the system-bath network also allows the number of degrees of freedom entangled in the system and bath configurations to be different. For the numerical treatment in this paper, the hydrogen transfer dimension is treated as the "transfer coordinate" whereas the orthogonal degrees of freedom are treated as bath and the $\bar{\alpha}_{T-B}$ correlators are determined by Schmidt decomposition.[21,23]

In this paper, all rank reductions constructed for eqs 1, 2, and 3 using the tensor networks, eqs 5, 6, 7, and 9, are performed using singular value decomposition (SVD) or Schmidt decomposition,[21,23] where, for example, in the first step:

$$\begin{aligned} C_{\bar{k}} &= \sum_{\alpha_1} C^{1}_{k_1,\alpha_1} \times \sigma^{1}_{\alpha_1} \times C_{\alpha_1,k_2,k_3,\cdots,k_{\mathcal{D}}} \\ &\equiv \sum_{\alpha_1} \tilde{C}^{1}_{k_1,\alpha_1} \times \tilde{C}_{\alpha_1,k_2,k_3,\cdots,k_{\mathcal{D}}} \end{aligned} \tag{11}$$

where $\{\sigma^{1}_{\alpha_1}\}$ are the singular values and $C^{1}_{k_1,\alpha_1}$ and $C_{\alpha_1,k_2,,k_3,\cdots,k_{\mathcal{D}}}$ are the left and right singular vectors when the tensor $C_{\bar{k}}$ has been folded in to a matrix with dimensions, $C_{k_1,[k_2\times k_3\times\cdots]}$. Further details regarding the algorithms used here may be found in ref 8. In the second part of the equation above, the square roots of the (positive definite) singular values are absorbed into the definition of the vectors and this is also similarly done in eqs 5 and 6. Using this general methodology, extended to higher order,[8,14,81] we are able to derive a general and adaptive scheme that reduces the complexity involved in storage of quantum mechanical data (wave functions and potential). Furthermore, the set of singular values $\sigma^{i}_{\alpha_i}$ probes the entanglement between the separated dimensions. This probe is directly reflected in the Schmidt decomposition. Therefore, α_i does not need to include all singular values and singular vectors generated but encompasses states that are most important to the recreation of the original function, $C_{\bar{k}}$. Determination of such states represented by $\bar{\alpha}$, and the associated singular values and singular vectors, allows one to gauge the correlation and entanglement between the various dimensions; for example, for the interesting situation where N_α is discovered to be of the order of unity, the

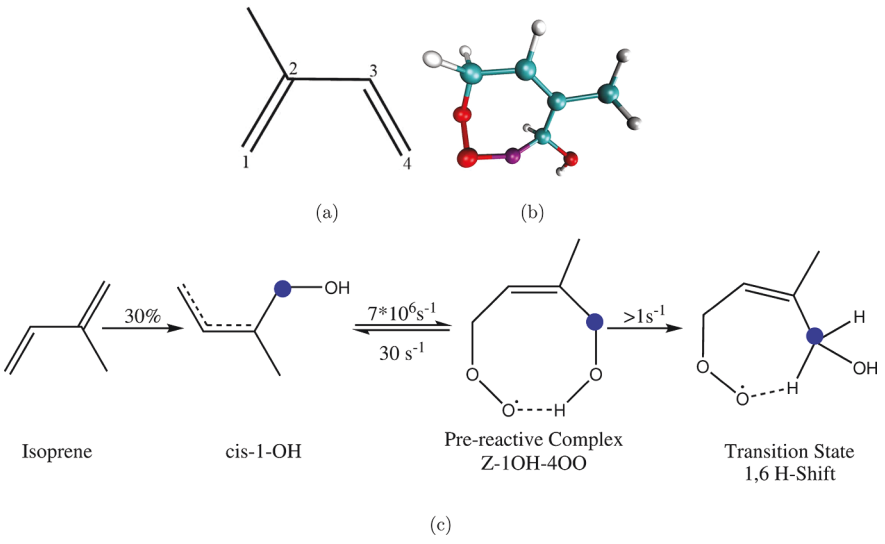

Figure 5. Isoprene (a), a volatile organic terpene that reacts with the HO$^{\bullet}$ radical and O_2 as per the mechanism presented in part c. The transition state obtained from the 1,6 hydrogen atom shift is shown in part b.

DOI: 10.1021/acs.jctc.8b01113
J. Chem. Theory Comput. 2019, 15, 2780−2796

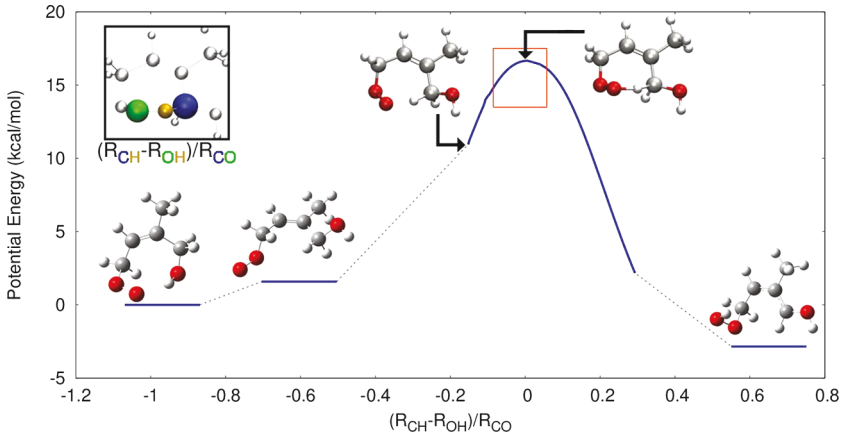

Figure 6. Transition state for the 1,6 hydrogen atom shift in the isoprene-hydroxy-peroxy (RO_2) radical is shown in Figure 5b. The corresponding energy profile along an intrinsic reaction coordinate is shown in part a here, with a prereactive complex at roughly −0.6 units along the dimensionless reaction coordinate. The curved region near the transition state that is shown in solid blue, is discretized along the reaction coordinate (defined pictorially in the figure legend provided on the top-left corner) and the shared hydrogen nucleus is treated quantum mechanically on a body-fixed grid based coordinate system that is further explained in Appendix A, with details in ref 42.

correlation is limited and a time-dependent self-consistent field-type approximation might suffice. Yet again, the power of this approach here is the fact that such a correlation, as we will see, is dynamical and could potentially change during a reactive process. Likewise, the potential energy surface may be similarly adapted by computationally gauging the correlation across dimensions.

III. BRIEF NOTE ON THE LEUVEN ISOPRENE MECHANISM 1 (LIM1)

The system used in this publication to gauge the efficiency and accuracy of the tensor networks methodology is the isoprene-hydroxy-peroxy (RO_2) radical system shown in Figure 5b. This radical is thought to be encountered[32,38−41] during the reaction of the $HO^{\bullet}$ radical and O_2 with the volatile organic terpene,[32−40,82] isoprene (Figure 5a). The RO_2 radical may isomerize through a hydrogen transfer process as outlined by the Leuven isoprene mechanism (LIM1)[32−40] a portion of which is captured in Figure 5c, with the transferring hydrogen atom highlighted using magenta in Figure 5b. The detailed reaction profile corresponding to the 1,6 hydrogen atom shift is shown in Figure 6 along with the prereactive complex. The LIM1 isomerization of RO_2 provides one possible explanation for the unexpectedly high $HO^{\bullet}$ radical concentrations found in atmospheric campaigns in rain-forest environments.[33−35] In urban areas, the RO_2 radical reacts with NO_X to produce $HO^{\bullet}$. However, in the rain-forested environments with low NO_X concentrations, production of the $HO^{\bullet}$ radical is not expected but is noted in recent environmental campaigns.[32−40] In the LIM1 mechanism (Figure 5c) an internal hydrogen shift in RO_2 leads to products that recreate $HO^{\bullet}$ radical without NO_X.[32,38−41]

In ref 42, reduced dimensional quantum-nuclear studies were conducted along the intrinsic reaction coordinate highlighted within the region shown in blue in Figure 5c. We analyzed the evolution of the reduced dimensional potential energy surfaces pertaining to the shared hydrogen nuclear degrees of freedom, details for which are in ref 42, with a summary in Appendix A. The reduced dimensions shown in Figure 5c were constructed as follows. First an intrinsic reaction coordinate was computed. This was done using standard methods available in electronic structure packages. Following this, at each geometry along the reaction coordinate in the blue region shown in Figure 6, a rectangular grid was constructed to represent the shared hydrogen nucleus as a quantum wave function in the coordinate representation. Details regarding the number of discrete samples utilized along the reaction coordinate and parameters pertaining to the quantum nuclear grid are given in Appendix A. Illustrations of the geometric evolution of the system along the intrinsic reaction coordinate and snapshots of the grid along the same are shown in Figure 7. Thus, a body-fixed grid representation for the shared hydrogen nucleus is constructed, and this representation is used to compute potential surface and eigenstates of the shared proton along the hydrogen-transfer

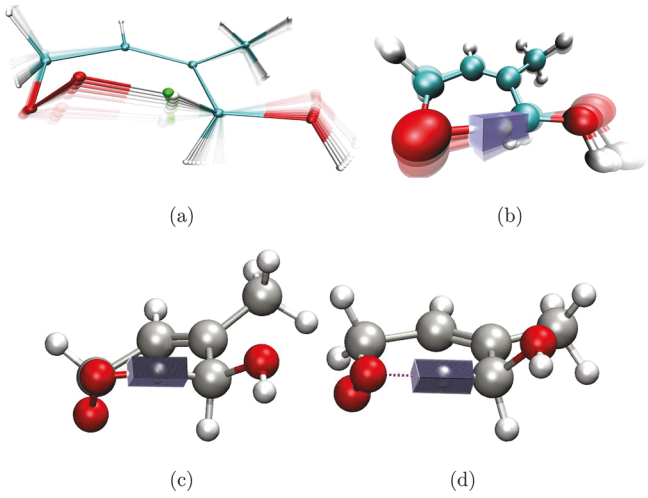

Figure 7. Evolution of the molecular network along the reaction coordinate shown in Figure 6 is depicted here in part a using overlapping images with the more transparent images occurring earlier during the reactive event and the solid geometries appearing closer to the transition state. The teal spheres in part a represent the centroid location corresponding to the ground hydrogen-nuclear eigenstate computed on the grid described in Appendix A. The grid itself evolves simultaneously along the reaction coordinate and such an evolution is shown with snapshots along the reaction coordinate in parts b−d. In this paper, the eigenstates for the transferring hydrogen nucleus and the associated potential energy surface are treated as tensor networks and used to compute product side probabilities.

DOI: 10.1021/acs.jctc.8b01113
J. Chem. Theory Comput. 2019, 15, 2780−2796

coordinate. In the remaining portion of this paper the nuclear wave functions and reduced dimensional potential energy surfaces thus obtained will be compressed using tensor networks to reproduce the transmission probabilities at much reduced computational cost.

IV. RIGOROUS BOUNDS AND ERROR ESTIMATES FOR THE TENSOR NETWORK REPRESENTATIONS FOR WAVE-FUNCTIONS AND POTENTIALS

As described in the previous section we probe the effect of nuclear quantization on the hydrogen transfer step in Figure 6. The shared proton degrees of freedom are discretized on a grid as in ref 42, and potentials were computed using the sampling functions as in ref 42. (Also, see Appendix A.) The reaction coordinate is incremented along the intrinsic reaction coordinate represented in Figure 6, and at each point along the intrinsic reaction coordinate, a reduced dimensional potential is computed and the accuracy of the reduced dimensional potential surface has been discussed in ref 42.

Here the tensor network forms of the hydrogen-nuclear eigenfunctions obtained along the reaction coordinate are used to treat the reactive process within an adiabatic approximation for separation of reaction coordinate and quantum nuclear degrees of freedom. It has been shown in previous publications[43,83] that as the system evolves along the intrinsic reaction coordinate in such hydrogen transfer problems the dynamics is nonadiabatic in the space of eigenstates belonging to the reduced degrees of freedom. But here we only concern ourselves with reducing the complexity associated with eigenstate and potential surface calculation and representation. The associated eigenfunctions and potential energy surfaces are approximated as tensor networks. In this section we present error estimates to gauge the accuracy and efficiency of the tensor network approximation for the eigenstates and potential surfaces.

To gauge the accuracy of the eigenstates there are essentially two ways to proceed. The true error in a tensor network wave function or potential is obtained only by comparison with the respective fully correlated counterpart

$$\Gamma_{\mathrm{Err}}^{N_{\bar{x}}:N_{\bar{x}}} \equiv \log_{10}\left(\sqrt{\int \mathrm{d}\bar{x}[\Psi(\bar{x}) - \lambda^{*}\Psi_{TN}^{N_{\bar{x}}:N_{\bar{x}}}(\bar{x})]^2}\right) \tag{12}$$

Here $N_{\bar{x}}$ is the total number of grid points, $\Psi_{TN}^{N_{\bar{x}}:N_{\bar{x}}}(\bar{x})$ is obtained from the tensor-network approximation to $\Psi(\bar{x})$ and λ is a phase factor that eliminates any phase differences between $\Psi(\bar{x})$ and $\Psi_{TN}^{N_{\bar{x}}:N_{\bar{x}}}(\bar{x})$. In the results section, $\Psi_{TN}^{N_{\bar{x}}:N_{\bar{x}}}(\bar{x})$ is created from $\Psi(\bar{x})$ through a sequence of singular value decompositions and hence λ is chosen to be one. However, computing eq 12 defeats the purpose of using tensor networks since it requires storage of an exponentially scaling number of function values that are enumerated on the grid $\bar{x}$. Thus, rigorous error estimates and error bounds are essential in gauging the accuracy and efficiency of the tensor network formalism without needing to compute the full dimensional wave function or potential.

To obtain general purpose error estimates we first begin by describing the error for a two-dimensional function that is decomposed through a single SVD or Schmidt decomposition.[21,23] Note that the first step in the system-bath decomposition in eq 9 is a single SVD; furthermore, eqs 5, 6, 7, and 10 are all a sequence of SVDs. Hence this two-dimensional discussion is of relevance and will be scaled to provide bounds and error-estimates to both MPS and system-bath configurations. In this case it follows that the error maybe obtained based on the singular values and singular vectors that are discarded based on a user defined error-threshold:

$$\Omega_{2D} = \sqrt{\left[\sum_{j=N_\alpha+1}^{N_1} (\sigma_j)^2\right]} \tag{13}$$

where N_1 and N_α are defined as in eq 8, namely, N_1 is the number of basis functions or grid points in each degree of freedom and is also the total number of singular values, N_α is the number of singular values retained based on the user defined error threshold, and σ_j are the associated set of singular values.

But beyond two-dimensions, the matrix product state factorization suffers from nonorthogonality of the internal physical dimensions.[8] This restricts the errors and provides upper bounds in $\mathcal{D}$-dimensions provided the function is normalized:[7,55,84]

$$\Omega_{\mathrm{MPS}} \equiv \sqrt{\sum_{i=1}^{\mathcal{D}-1}\left[\sum_{j=N_\alpha^i+1}^{N_i} (\sigma_j^i)^2\right]} \tag{14}$$

where N_i is the number of grid points or basis functions along dimension i and N_α^i is the number of retained singular values for the SVD separating the ith and $(i+1)$th dimensions. Thus, the order of magnitude of this upper bound is captured here using

$$\Gamma_{\mathrm{MPS}} = \log_{10}(\Omega_{\mathrm{MPS}}) \tag{15}$$

The error for the system-bath partitioned tensor network can be obtained using eq 13, since the system-bath partition, as noted above, is composed of a single SVD followed by two different MPS factorizations that are now dependent on the number of singular values retained during the first SVD. Hence we may write the upper bound using the omitted singular values as

$$\Gamma_{SB} \equiv \log_{10}\left(\left\{\left[\sum_{i=\alpha_{T-B}+1}^{\mathcal{D}^{T-B}} (\sigma_i^{T-B})^2\right] + \sum_{l=1}^{\alpha_{T-B}} (\sigma_l^{T-B})^2 \times \left[\sum_{\tau=1}^{\mathcal{D}^T}\sum_{j=\alpha_{l,\tau}^T+1}^{N_{l,\tau}^T} (\sigma_{j,\tau,l}^T)^2 + \sum_{\xi=1}^{\mathcal{D}^B}\sum_{k=\beta_{l,\xi}^B+1}^{N_{l,\xi}^B} (\sigma_{k,\xi,l}^B)^2\right]\right\}^{1/2}\right) \tag{16}$$

Here the first square bracketed term, $[\cdots]$, is the error for the system-bath separation with α_{T-B} being the number of correlation dimensions retained between the system and bath degrees of freedom. Consequently, the discarded singular values and singular vectors, $[(\alpha_{T-B}+1)\cdots \mathcal{D}^{T-B}]$, constitute the error from the first square bracketed term and is based on similar arguments as in eq 13. The term following the first square bracketed term is the weighted MPS error for the two respective system and bath MPS factorizations similar to eq 14 that are now, however, attenuated by the respective, retained, system-bath singular values $\{\sigma_l^{T-B}\}$; the first term being the error in $\mathcal{D}^T$-system dimensions and similarly the second term being the error in $\mathcal{D}^B$-bath dimensions, both analogous to eq 14.

In the results section, we consider the hydrogen transfer reaction discussed above and in Appendix A, which comprises a three-dimensional wavepacket evolving along a classically

DOI: 10.1021/acs.jctc.8b01113
J. Chem. Theory Comput. 2019, 15, 2780−2796

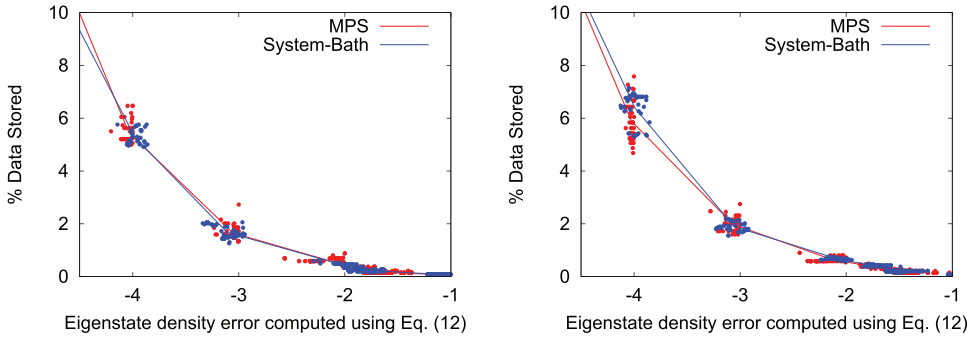

(a)Ground hydrogen-nuclear eigenstate (b)First excited hydrogen-nuclear eigenstate

Figure 8. Eigenstate data storage as a function of error threshold given by eq 12. See text for details.

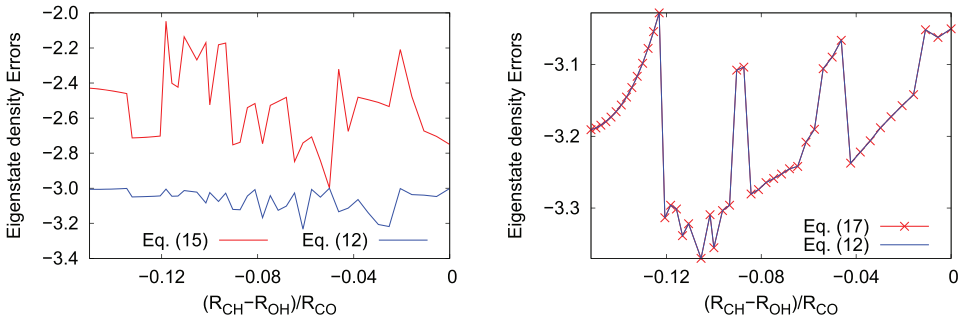

(a)MPS (b)System-Bath

Figure 9. Blue trace is the error in ground eigenstate (as per eq 12) as a function of reaction coordinate. This does require exponential scaling storage as discussed earlier. The red curve is the error estimate that is calculated using eq 15 for part a and using eq 17 for part b. As is clear, eq 15 provides an upper bound (as already noted in ref 84) and eq 17 provides a much better error estimate, both of which do not require exponential scaling storage as discussed earlier.

treated hydrogen transfer reaction coordinate. In addition to using MPS to factorize this wavepacket along the transfer coordinate (which would need errors to be monitored using eqs 14 and 15), we also use a system-bath separation to probe the use of eq 16. In that case the system coordinate is the donor−acceptor direction and the two orthogonal coordinates are treated as bath. Hence, eq 16 simplifies to

$$\Gamma_{3D,SB} = \log_{10}\left(\left\{\left[\sum_{i=\alpha_{T-B}+1}^{D^{T-B}} (\sigma_i^{T-B})^2\right] + \left[\sum_{l=1}^{\alpha_{T-B}} (\sigma_l^{T-B})^2 \times \sum_{k=\beta_l^B+1}^{N_l^B} (\sigma_{k,1,l}^B)^2\right]\right\}^{1/2}\right) \quad (17)$$

Again the first square bracket contains the error associated with the system-bath separation and the second square brackets is the weighted error for the bath variables. Equations 14, 15, and 17 are used in the next section to gauge the accuracy of the tensor network formalism.

V. TENSOR NETWORK FORMS OF EIGENSTATES, POTENTIAL SURFACES, AND WAVEPACKET TRANSMISSION AMPLITUDES

We proceed to compute and evaluate tensor network approximations to the quantum nuclear eigenstates along the hydrogen-transfer coordinate depicted in Figure 6. As noted in Appendix A, we sample the reaction coordinate at 48 different locations and use the reduced dimensional potential surfaces at the respective geometries as obtained in ref 42 to compute a range of hydrogen nuclear eigenstates. We then compute MPS and system-bath tensor network representations for each of the eigenstates at these 48 geometries, and in Figure 8 we present the behavior of wavepacket data compression and accuracy, as dictated by eq 12, for the ground and first excited states. Specifically the left vertical axis in Figure 8 represents the percentage of data stored and the horizontal axis represents the error in eigenstate density as given by eq 12 for all geometries. This is done for four different error threshold values: $\Gamma_{\mathrm{Err}}^{N_{\bar{\alpha}}:N_{\bar{x}}} < -4$, $\Gamma_{\mathrm{Err}}^{N_{\bar{\alpha}}:N_{\bar{x}}} < -3$, $\Gamma_{\mathrm{Err}}^{N_{\bar{\alpha}}:N_{\bar{x}}} < -2$, and $\Gamma_{\mathrm{Err}}^{N_{\bar{\alpha}}:N_{\bar{x}}} < -1$. These four error thresholds represent the order of magnitude of the L^2 norm of the difference between the multiconfigurational form of the wave function and its tensor network counterpart as seen in eq 12. Clearly, both MPS and system-bath network methods are extremely efficient for a range of eigenstate. With only 2% of data most eigenstates are captured to within eigenstate accuracy loss of less than 0.1%. This implies an eigenstate probability loss of only 10^{-3}. One percent accuracy in eigenstate value (that is 10^{-2}% error in eigenstate probability) can be obtained by storing only 0.5% of the data.

In Figure 9 we compare the development of the error bounds in eqs 14, 15, and 17 with the explicit errors given by eq 12 as a function of reaction coordinate for the threshold value of $\Gamma_{\mathrm{Err}}^{N_{\bar{\alpha}}:N_{\bar{x}}} < -3$. Clearly, eq 15 presents an upper bound to the true error as already stated, but the system bath value, eq 17, provides a much closer estimate of the true error. The reason for this is

DOI: 10.1021/acs.jctc.8b01113
J. Chem. Theory Comput. 2019, 15, 2780−2796

purely problem choice. For the situation here, with one proton in three-dimensions, with donor−acceptor coordinate defined as the system coordinate, and the two orthogonal coordinates defined as bath variables, the system bath partition essentially includes the sum over two independent SVDs as is apparent from eq 17. Since the error estimate for a single SVD computed using the discarded singular values is essentially exact, as noted in the discussion before eq 13, the system-bath estimate, eq 17, provides a closer agreement with the true error in eq 15.

We next address the issue of uniqueness in these tensor network decompositions. It must also be noted that, while the specific choice of singular values that leads to the errors above is unique, this does depend on the choice of tensor network and the arrangements of dimensions within each tensor network. For example, the MPS error depends on whether the donor−acceptor dimension is dis-entangled first, through the first SVD, or later in the tensor decomposition. This can clearly be seen from eq 5 which depicts a logical arrangement of dimensions. While, in the above results the donor−acceptor dimension was taken to be the first dimension to be dis-entangled, one may also ask whether the errors are still well-behaved when the physical dimensions are permuted. This is precisely the question addressed in Figure 10. Clearly, while the errors are different, all permuted versions of MPS lead to similar errors.

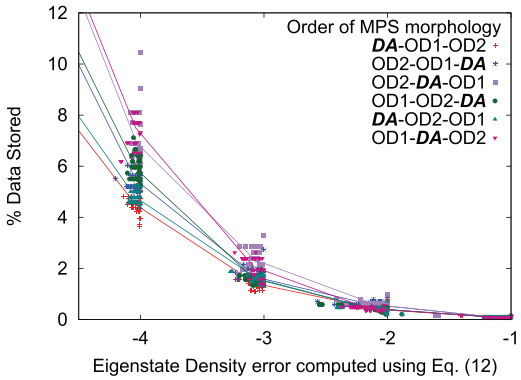

Figure 10. Eigenstate data storage as a function of error threshold given by eq 12 for various permuted versions of the MPS morphology. For example, the donor−acceptor (DA) hydrogen transfer direction may be featured as one of the peripheral directions of the MPS (the color keys with DA at the beginning or the end) or the donor−acceptor direction may be the central MPS dimension. In all cases the two orthogonal dimensions (OD1 and OD2) may in turn be permuted, and for all permuted sets the compression and accuracy are quite similar.

To make this approach computationally useful and to reduce the scaling of (a) eigenstate calculations, (b) quantum propagation, and (c) computing measurable quantities, in the remaining portion of this paper, we show how (i) product side probabilities may be computed through reduced scaling methods that employ tensor networks and (ii) potential surface data can be compressed using the tensor network formalism. In Appendix B we will explore the theoretical rationale that allows efficient quantum dynamics.

V.A. Product Side Probabilities and Reaction Probabilities. We have computed the tensor network forms of the ground and excited state wave functions above, along an intrinsic reaction coordinate, and have showed this process to be an efficient way to store quantum mechanical data. As stated earlier, it has been shown in previous publications[43] that as the system evolves along the intrinsic reaction coordinate in such hydrogen transfer problems the dynamics is nonadiabatic in the space of eigenstates belonging to the reduced degrees of freedom. But here we only concern ourselves with reducing the scaling of computing transmission properties, that is, the product side probabilities. Toward this we introduce the MPS form of a final product state basis function, $\Upsilon_f(\bar{x})$, to reduce the scaling of computing wavepacket probabilities on the product side, that is, $\langle \Upsilon_f|\rho_0\rangle \equiv \langle \Upsilon_f||\Phi_0|^2\rangle$, where

$$\Upsilon_f(\bar{x}) = \sum_{\bar{\beta}} \left[\eta^1_{\beta_1}(x_1) \times \left\{ \prod_{i=2}^{\mathcal{D}-1} \eta^i_{\beta_{i-1},\beta_i}(x_i) \right\} \times \eta^{\mathcal{D}}_{\beta_{\mathcal{D}-1}}(x_{\mathcal{D}}) \right] \tag{18}$$

and the associated product side probability may be written as

$$\begin{aligned} \langle \Upsilon_f|\rho_0\rangle = \Bigg\{ \sum_{\substack{\alpha_{\mathcal{D}-1} \\ \beta_{\mathcal{D}-1}}} \Bigg[\int \mathrm{d}x_{\mathcal{D}} \eta^{\mathcal{D}-1}_{\beta_{\mathcal{D}-1}}(x_{\mathcal{D}}) \\ \times \Bigg\{ \cdots \Bigg[\int \mathrm{d}x_2 \eta^2_{\beta_2,\beta_1}(x_2) \times \Bigg\{ \sum_{\beta_1,\alpha_1} \Bigg[\int \mathrm{d}x_1 \eta^1_{\beta_1}(x_1) \times \varrho^1_{\alpha_1}(x_1) \Bigg] \Bigg\} \\ \varrho^2_{\alpha_1,\alpha_2}(x_2) \Bigg] \cdots \Bigg\} \varrho^{\mathcal{D}-1}_{\alpha_{\mathcal{D}-1}}(x_{\mathcal{D}}) \Bigg] \Bigg\} \end{aligned} \tag{19}$$

where $\{\varrho_{\alpha_1}; \varrho^{i+1}_{\alpha_i,\alpha_{i+1}}; \varrho^{\mathcal{D}-1}_{\alpha_{\mathcal{D}-1}}\}$ are the tensor components of ρ_0. Significantly, while the left side encodes an exponential scaling operation, the right side scales as

$$\sum_i \beta_i \times \alpha_i \times N_1 \approx O(N_1) \tag{20}$$

where N_1 is the size of each individual dimension, and the approximate scaling on the right side is only true for $\{\beta_i,\alpha_i\} \ll N_i$, that is, we have utilized the area law of quantum entanglement.[14,19,20,85] In eq 19, the square bracketed terms, $[\cdots]$, include inner-products over individual physical dimensions, whereas the curly bracketed terms, $\{\cdots\}$, include summations over the relevant internal correlator dimensions. Furthermore, the set of values $\{\beta_i\}$ and $\{\alpha_i\}$ do not need to be the same and the two functions may have arbitrarily different internal entanglements captured in an adaptive fashion through sequential SVD as noted above. A visual representation of eq 19 is provided in Figure 11. Here, for example, the blue tensor network (top) is the eigenstate and the black (bottom) tensor network is the product state basis. As indicated, these interact through the shared physical dimensions, $\bar{x}$. Each physical dimension is separately integrated and the entanglement dimensions are processed in a sequential fashion visually demonstrated in Figure 11. This allows the use of reduced storage tensor networks here to calculate transition probabilities.

In Figure 12, we gauge the accuracy of the product side probabilities computed using MPS and compare these to the results obtained from the full grid quantum nuclear wavepacket. It is clear that the difference between the two methods is approximately three-orders of magnitude lower as compared to the actual product side probability. The accuracy is very high for these calculations at much reduced computational cost.

V.B. Tensor Network Representation of Potential Energy Surfaces. A critical piece of the effort in quantum

DOI: 10.1021/acs.jctc.8b01113
J. Chem. Theory Comput. 2019, 15, 2780−2796

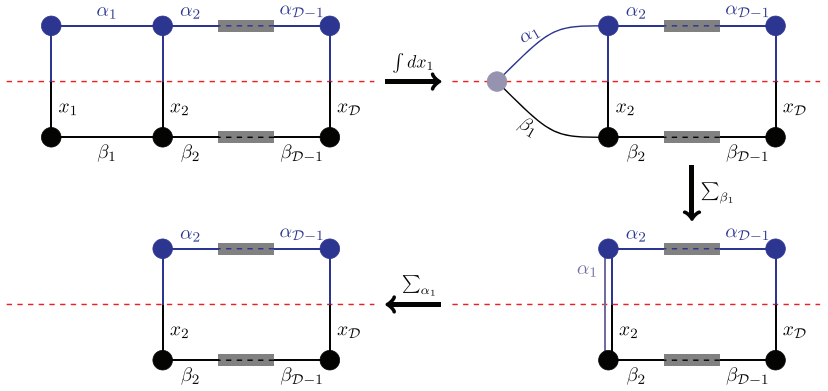

Figure 11. Inner product of two MPS networks, eq 19, leads to the product side probabilities shown in Figure 12. The red line separates the wave packet density (blue) from the product state basis (black). The figure also shows the sequence of operations in the inner product that leads to a reduced scaling algorithm. These steps are derived from those discussed in ref 42.

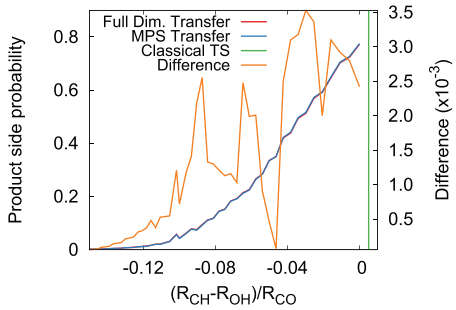

Figure 12. Comparison of the total probability on the product side as given by eq 19 and Figure 11. "Full Dim. Transfer" implies the product side probabilities computed by using the full grid wavepacket, and the inner product is then an exponential scaling operation in dimensionality. "MPS transfer" implies, using the right side of eq 19 to compute the product side probabilities. "Difference" includes the difference between the two and is shown on the right vertical axis. *The difference is 3 orders of magnitude smaller than product side probability.* Clearly the accuracy from using MPS, eq 19, and the algorithm depicted in Figure 11 is very high and at much reduced computational effort.

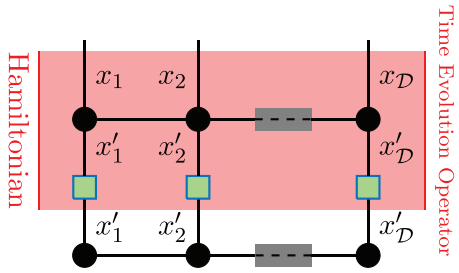

Figure 13. Action of the Hamiltonian (and by extension the time-evolution operator) on an initial wavepacket may be simplified through an MPS form of the Hamiltonian/Propagator along with the methods outlined in Figure 11 and eq 19. Also see Appendix B.

dynamics involves the action of the Hamiltonian and/or the propagator on a wave packet. We have shown above that the wave packet maybe adaptively compressed by gauging the entanglement through tensor networks. Furthermore, product-side probabilities can also be computed by exploiting the same idea and in this case the topology of the tensor network (that is MPS or system-bath network) is maintained the same for the two functions used in the inner product. But, it is also required that we consider a similar representation of the Hamiltonian and propagator, that is the kinetic and potential energy operators, to allow efficient scaling of quantum dynamical and eigen-energy calculations. In doing so, we may construct reduced scaling algorithms for propagation and eigenstate calculations as is done for the product side probability in eq 19 and in Figure 11. In Figure 13, the wave packet is shown as a rank-$\mathcal{D}$ MPS tensor and by extension the Hamiltonian/Propagator, a rank-$2\mathcal{D}$ tensor is also presented as a tensor network. In this situation, the complexity of the action of the Hamiltonian/Propagator on the wavepacket may be reduced as suggested by Figure 13 and along the lines of eqs 19 and 20. In Appendix B we formally outline the critical steps involved in carrying out such operations at reduced complexity. Importantly, for the "Distributed Approximation Functional" (DAF)[86−88] form of the free propagator in eq 2 and the DAF form of the kinetic energy operator in eq 1, the action of the kinetic energy on an MPS wave function is a sum of tensor products, eq 3, and the action of the free-propagator is an independent set of tensor products in eq 4. Specifically, differentiated forms of the one-dimensional functions are retained to compute the action of the kinetic energy (eq 1), and similarly, free-propagated forms of the one-dimensional functions are retained to put together the action of the free-propagator (eq 4).

As a step in this general direction, we now express potential energy surfaces as tensor networks. Our approach has close connections and is complementary to many other approaches used in the community including the sum over product approximations,[89] product approximations in POTFIT,[57,68−71] and tensor train methods.[90] Here we utilize the MPS and system-bath tensor networks to obtain suitable representations of the potential energy surface data. Our approach differs in spirit from those in refs 57, 68−71, 89, 91, and 92 in that degrees of freedom are entangled in smaller sets as may be noted from the MPS approximation for the potential in eq 3 written in eq 7. This is also clear when we explicitly rewrite eq 7 as

$$\mathbf{V}(\bar{x}_0) = \sum_{\alpha_{\mathcal{D}-1}} \cdots \left[\sum_{\alpha_3} \left[\sum_{\alpha_2} \left[\sum_{\alpha_1} \mathcal{V}^1_{\alpha_1}(x^0_1) \times \mathcal{V}^2_{\alpha_1,\alpha_2}(x^0_2) \right] \right. \right.$$
$$\left. \left. \mathcal{V}^3_{\alpha_2,\alpha_3}(x^0_3) \right] \mathcal{V}^4_{\alpha_3,\alpha_4}(x^0_4) \right] \cdots \mathcal{V}^{\mathcal{D}}_{\alpha_{\mathcal{D}-1}}(x^0_{\mathcal{D}}) \tag{21}$$

which clarifies the local correlations captured in Figure 2. Of course, in suitably representing eq 21, we must choose an

DOI: 10.1021/acs.jctc.8b01113
J. Chem. Theory Comput. 2019, 15, 2780−2796

ordered set, $\bar{\alpha} \equiv \{\alpha_1, \alpha_2, \cdots, \alpha_i, \cdots\}$ which defines the neighborhood of correlation as is clear from eq 21 and in this sense, eq 21 has close connections to approximations used in ML-MCTDH. In this paper this set is ordered as per the degrees of freedom of the transferring hydrogen nucleus that is quantized here. (Permuted forms are also considered here in the spirit of Figure 10.) Likewise, a system bath version of the potential surface is also used here and maybe written analogous to eqs 9 and 10 as

$$\begin{aligned}\mathbf{V}(\bar{x}) = \sum_{\bar{\alpha}_{T-B}} \Bigg[\sum_{\bar{\alpha}} \Bigg[& \mathcal{V}^{1,\bar{\alpha}_{T-B},T}_{\alpha_1}(x^0_{T,1}) \\ & \times \left\{ \Pi_{i=2}^{\mathcal{D}^T-1} \mathcal{V}^{i,\bar{\alpha}_{T-B},T}_{\alpha_{i-1},\alpha_i}(x^0_{T,i}) \right\} \times \mathcal{V}^{\mathcal{D}^T,\bar{\alpha}_{T-B},T}_{\alpha_{\mathcal{D}^T-1}}(x^0_{T,\mathcal{D}^T}) \Bigg] \\ & \times \sum_{\bar{\mu}} \Bigg[\mathcal{V}^{1,\bar{\mu}_{T-B},B}_{\mu_1}(x^0_{B,1}) \times \left\{ \Pi_{i=2}^{\mathcal{D}^B-1} \mathcal{V}^{i,\bar{\mu}_{T-B},B}_{\mu_{i-1},\mu_i}(x^0_{B,i}) \right\} \\ & \times \mathcal{V}^{\mathcal{D}^B,\bar{\mu}_{T-B},B}_{\mu_{\mathcal{D}^B-1}}(x^0_{B,\mathcal{D}^B}) \Bigg] \Bigg] \end{aligned} \tag{22}$$

In Figure 14, we present the extent of data compression as a function of error computed along the lines of eq 12, that is

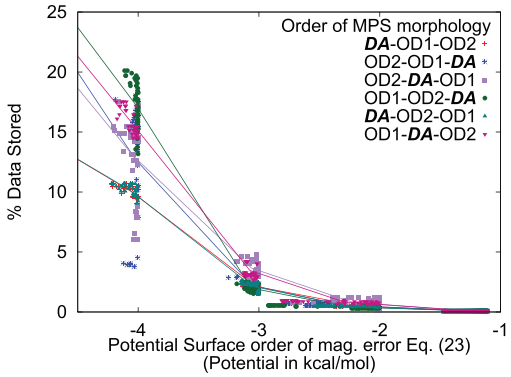

Figure 14. Potential surface data storage as a function of error threshold given by eq 23 for various permuted versions of the MPS morphology. For example, the donor−acceptor (DA) hydrogen transfer direction may be featured as one of the peripheral directions of the MPS (the color keys with DA at the beginning or the end) or the donor−acceptor direction may be the central MPS dimension. In all cases the two orthogonal dimensions (OD1 and OD2) may in turn be permuted, and for all permuted sets the compression and accuracy are quite similar.

$$\Gamma^{\mathrm{Pot},N_{\bar{\alpha}};N_{\bar{x}}}_{\mathrm{Err}} = \log_{10}\left(\frac{1}{N_{\bar{x}}} \times \sqrt{\int \mathrm{d}\bar{x} [\mathbf{V}(\bar{x}) - \mathbf{V}^{N_{\bar{\alpha}};N_{\bar{x}}}_{TN}(\bar{x})]^2} \right) \tag{23}$$

The errors are presented in Figure 14 for all permuted forms of the MPS. Clearly the accuracy is very high. An RMS error of 10^{-2} kcal/mol may be achieved through less than 1% of the potential energy data as clear from the value of the ordinate in Figure 14 for the abscissa value of "−2". This is the case for all permuted forms of the MPS.

In Figure 15, we present the error in potential surfaces as a function of the reaction coordinate when the order of magnitude of the error reflected by the expression in eq 23 is chosen to be "−3". This reflects an RMS error of approximately 10^{-3}. As seen in Figure 15, the potential energy surface compression is still good, for this stringent and error threshold. But, as noted before, the error in eq 23 requires the full grid potential. Hence, consistent with eq 15, here since the potential is *not* a normalized quantity (unlike the wavepacket was in eq 15), error estimates may be introduced that do not require *a priori* knowledge of the grid potential and these are given by

$$\begin{aligned}\Gamma^{\mathrm{Pot}}_{\mathrm{MPS}} &= \log_{10}\left(\frac{1}{N_{\bar{x}}} \times \sqrt{\sum_{i=1}^{\mathcal{D}-1} \left[\sum_{j=N^i_\alpha+1}^{N^i_T} (\sigma^i_j)^2 \right]} \right) \\ &= \frac{1}{2}\log_{10}\left(\sum_{i=1}^{\mathcal{D}-1} \left[\sum_{j=N^i_\alpha+1}^{N^i_T} (\sigma^i_j)^2 \right] \right) - \log_{10} N_{\bar{x}} \end{aligned} \tag{24}$$

for the MPS case and the corresponding system-bath version of error bounds are

$$\begin{aligned}\Gamma_{SB} \equiv \log_{10}\Bigg(\frac{1}{N_{\bar{x}}} \Bigg[& \Bigg[\sum_{i=\alpha_{T-B}+1}^{D^{T-B}} (\sigma_i)^2 \Bigg] + \sum_{l=1}^{\alpha_{T-B}} (\sigma_l)^2 \\ & \Bigg[\sum_{\tau=1}^{\mathcal{D}^T} \sum_{j=\alpha_l^T+1}^{N_l^T} (\sigma^T_{j,\tau,l})^2 \\ & + \sum_{\xi=1}^{\mathcal{D}^B} \sum_{k=\beta_l^B+1}^{N_l^B} (\sigma^B_{k,\xi,l})^2 \Bigg]^{1/2} \Bigg] \Bigg) \end{aligned} \tag{25}$$

As noted in Figures 15 and 16, the accuracy is high and the amount of data that is stored is a small fraction of the grid. Again the MPS error estimate, eq 24, and the system-bath version, eq 25, provide a tight estimate and may be used in practical computations.

One way of interpreting eqs 7, 21, and 22 is as an adaptive generation of a set of one-dimensional basis functions, $\{\mathcal{V}_{\alpha_{i-1},\alpha_i}(x_i)\}$, $\{\mathcal{V}^{i,\bar{\alpha}_{T-B},T}_{\alpha_{i-1},\alpha_i}(x_{T,i})\}$, and $\{\mathcal{V}^{i,\bar{\alpha}_{T-B},B}_{\alpha_{i-1},\alpha_i}(x_{B,i})\}$ that capture the correlation across "neighboring dimensions" through summation across the respective entanglement indices. Indeed as per Figures 15 and 16, these ideas do capture the complexities of the potential quite well and in future we will use this (a) for multidimensional, multiparticle potentials and (b) along with the ansatz in Figure 13 and in Appendix B, for quantum nuclear dynamics.

VI. CONCLUSIONS

In this paper, we present two different tensor network topologies to represent the quantum nuclear wavepacket and potential energy surfaces and demonstrated these for the study of hydrogen transfer problems where quantum nuclear effects may be significant. One form of tensor network is the well-known matrix product state whereas the other form is one that represents a system-bath partitioned tensor network. In the latter, two different matrix product states are entangled in a "mean-field" fashion and can be thought of as "averaged" form of the previously known projected entangled pair states (PEPS)[14,59] tensor network. However, the system-bath partitioned tensor network also differs from a mean-field adapted PEPS network in that the number of degrees of freedom entangled in the system and bath configurations could be different. The approach developed here is used to compute the hydrogen-nuclear eigenstates and potential energy surfaces encountered during the hydrogen transfer process in the oxidation of a volatile organic compound called isoprene. Indeed we find that the networks studied are extremely efficient

DOI: 10.1021/acs.jctc.8b01113
J. Chem. Theory Comput. 2019, 15, 2780−2796

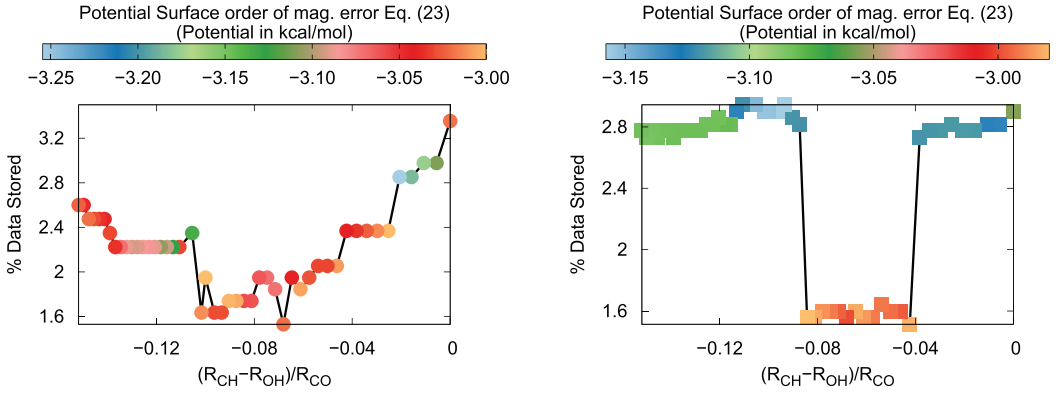

(a) (b)

Figure 15. Potential energy surface storage and accuracy along the hydrogen transfer reaction coordinate: MPS representation of the potential in part a and system bath representation in part b. The color represents the error in potential as per eq 23. The horizontal axis is the value along the reaction coordinate, and the vertical axis shows the percentage of data stored using the tensor network formalism. As can be seen a very low fraction of the data needs to be stored to obtain the necessary accuracy.

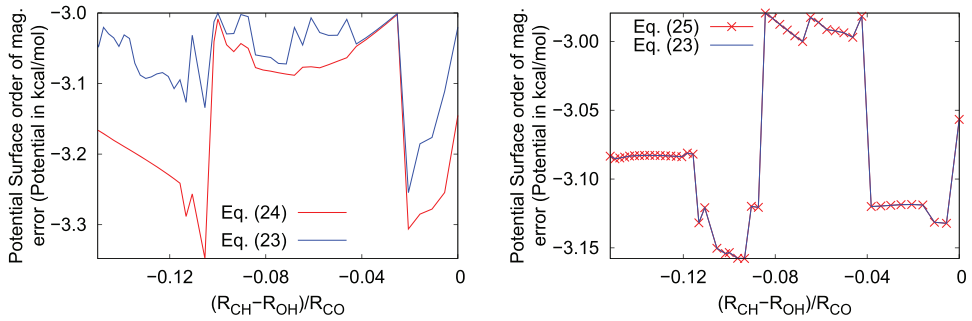

(a)MPS (b)System-Bath

Figure 16. Blue trace is the error in potential as per eq 23 as a function of reaction coordinate for the hydrogen transfer step shown in Figure 7a. This does require exponential scaling storage as discussed earlier. The red curve is the error estimate that is calculated using eq 24 for part a and using eq 25 for part b, both of which do not require exponential scaling storage.

Table 1. Grid Characteristics along the Reaction Coordinate

Number of slices along the reaction coordinate	48
Total number of grid points per slice	232897
Required number of electronic structure calculations	11,179,056
level of theory	B3LYP/6-311++g(d,p)
Average Number of electronic structure calculations performed, per IRC slice, when grid significance is gauged using ω_s [a]	373
Efficiency afforded theough use of ω_s	10^3

[a]Grid compression was not performed along the reaction coordinate dimension.

in compressing quantum nuclear wave function and potential energy surface data, without much of a compromise in accuracy. In addition we have provided a recipe to construct adaptive quantum dynamics, where changes in entanglement may be gauged on-the-fly. These aspects will be further probed in future publications.

APPENDIX A. BRIEF SUMMARY OF THE POTENTIAL ENERGY SURFACES, REACTION COORDINATES AND QUANTUM NUCLEAR EIGENSTATES FOR THE ISOPRENE-HYDROXY-PEROXY RADICAL

In ref 42, we analyzed the evolution of the reduced dimensional potential energy surfaces pertaining to the shared hydrogen nuclear degrees of freedom for the isoprene-hydroxy-peroxy radical system discussed in the earlier sections in this paper. The

DOI: 10.1021/acs.jctc.8b01113
J. Chem. Theory Comput. 2019, 15, 2780−2796

associated reaction profile is also shown in detail in Figure 6. The reduced dimensions were constructed as follows: First an intrinsic reaction coordinate was computed. This was done using standard methods available in electronic structure packages. Following this, at each geometry along the reaction coordinate, a rectangular grid was constructed to represent the shared hydrogen nucleus as a quantum wave function in the coordinate representation. As a result, a body-fixed grid representation for the shared hydrogen nucleus is obtained, and this body-fixed grid representation is depicted in Figure 7b–d for points along the reaction coordinate. The discretization parameters associated with such a grid representation and information regarding the intrinsic reaction coordinate are shown in Table 1.

A grid-based reduced dimensional Hamiltonian is introduced to represent the shared hydrogen nucleus

$$\mathcal{H}(\bar{x}, \bar{x}'; \mathbf{R_C}) = \mathcal{K}(\bar{x}, \bar{x}'; \mathbf{R_C}) + \mathbf{V}(\bar{x}; \mathbf{R_C}) \tag{A1}$$

where $\bar{x}$ is the grid representation of the reduced nuclear degrees of freedom and $\mathbf{R_C}$ represents the remaining degrees of freedom for a specific point along the intrinsic reaction coordinate. The kinetic energy operator, $\mathcal{K}(\bar{x}, \bar{x}'; \mathbf{R_C})$, is written using distributed approximating functionals (DAFs)[86−88] which provide an efficient banded Toeplitz matrix representation for the kinetic energy operator and the free-propagator. Critical aspects regarding the DAFs as these pertain to tensor networks are discussed in further in Appendix B. The term $\mathbf{V}(\bar{x}; \mathbf{R_C})$ is the potential obtained using electronic structure. The process, however, requires a potential surface, which consists of potential energy values at every point inside the grid, at all points along the intrinsic reaction coordinate; based on Table 1, this amounts to the prohibitive task of requiring roughly 11-million electronic structure calculations to describe the entire reaction coordinate. Furthermore, the number of such calculations grows exponentially with increase in quantum nuclear dimensions as already discussed following eq 7.

To simplify the problem, in ref 42, we used a Shannon entropy based sampling function that was originally developed in refs 93−95. We utilize this sampling function to gauge critical regions of the surface where electronic structure calculations must be done. The form of the sampling functions employed in ref 42 are

$$\omega_S(\bar{x}) \propto \frac{\tilde{S}[\rho(\bar{x})] + 1}{\tilde{\mathbf{V}}(\bar{x}) + 1} \tag{A2}$$

$$\omega_\rho(\bar{x}) \propto \frac{[\tilde{\rho}(\bar{x}) + 1/I_\rho][\nabla_{\bar{x}}\tilde{\mathbf{V}}(\bar{x}) + 1/I_{V'}]}{\tilde{\mathbf{V}}(\bar{x}) + 1/I_V} \tag{A3}$$

where, the quantum nuclear wave packet density, ρ, the potential surface, $\mathbf{V}$, the gradient of the potential, $\nabla_{\bar{x}}\mathbf{V}(\bar{x})$, and the *local* Shannon entropy function computed from the quantum wave packet density, $S[\rho(\bar{x})] \equiv -\rho(\bar{x})\log(\rho(\bar{x}))$, are all normalized, scaled, and shifted according to, for example

$$\tilde{\rho}(\bar{x}) = \frac{\rho(\bar{x}) - \rho_{\min}}{\rho_{\max} - \rho_{\min}} \tag{A4}$$

where $\rho_{\min}$ ($\rho_{\max}$) are the minimum (maximum) values for the wave packet density and similarly for $\tilde{\mathbf{V}}$, $\nabla_{\bar{x}}\tilde{\mathbf{V}}$, and $\tilde{S}[\rho(\bar{x})]$. This results in balanced contributions from each physical quantity. Furthermore, both sampling functions above remain positive semidefinite under this choice. Three integers I_ρ, $I_{V'}$, and I_V are chosen to be 1, 3, and 1, respectively, as outlined through analytical and numerical considerations in ref 93. We require the ω_ρ to have equal sampling in the classically allowed and classically forbidden regions of the potential, and this condition, and this alone, in ref 93 leads to the mentioned values of I_ρ, $I_{V'}$, and I_V. Furthermore, it was also shown in ref 42 that eq 2 captures the high frequency regions of the potential, as well as the low energy regions of the potential quite well and was found to be proportional to a spatially local Nyquist frequency[67] of the potential. That is

$$\omega_S(\bar{x}) \propto \frac{\mathcal{N}(\bar{x}; \omega)}{V(\bar{x})} \tag{A5}$$

where

$$\mathcal{N}(\bar{x}; \omega) = \int \mathrm{d}\bar{x}'\Theta(\delta - |\bar{x} - \bar{x}'|)\tilde{\mathbf{V}}(\bar{x}')\exp(\iota\omega\bar{x}') \tag{A6}$$

and appears to capture the "optimal" sampling necessary for a reasonably accurate potential surface. As per the Nyquist–Shannon sampling theorem,[65−67] any function that is band limited in the frequency domain, can be represented exactly using a finite number of samples in real space, provided the sampling rate is commensurate with the Nyquist frequency (eq 6) of the original function. It appears from ref 42 that eq 2 does capture the local variations of the Nyquist frequency accurately, and this aspect was used to obtain accurate and efficient samples of the potential with paramenters noted in Table 1. In the language of finite-element-methods used in computational mechanics, it may be noted that the TDDS method is an adaptive (*space and time dependent*) *h*-type mesh refining technique.[96] This process reduces the number of electronic structure calculations by 3−4 orders of magnitude. But the result is a set of electronic structure energies and gradients that are distributed on an irregular grid. We then interpolate to the full potential surface using four different fitting procedures in ref 42. The results from a geometric tiling of the potential surface[42] attenuated by locally independent Hermite curve interpolation[67,97] are used in section V.B to construct tensor decompositions. Furthermore, the potentials are also used to compute nuclear eigenstates from the Hamiltonian above and to also propagate the wavepacket and the former is used in section IV to compute tensor network approximations.

APPENDIX B. EFFICIENT PROPAGATION AND ACTION OF HAMILTONIAN ON A WAVEPACKET USING TENSOR-DECOMPOSED DISTRIBUTED APPROXIMATING FUNCTIONALS (DAFS)

The basis used is a grid basis which naturally partitions into a direction that is along the donor–acceptor axis and others that are orthogonal to this direction. This provides the rationale for the system-bath partitioned tensor network discussed in the paper, where the dimension along the donor–acceptor axis is interpreted as the system and orthogonal axes are represent as the bath. The matrix product state, by extension is constructed in two different ways. In one case the donor–acceptor dimension appears as one of the peripheral tensors coupling explicitly with only one of the orthogonal dimensions, whereas in the other situation the donor–acceptor dimension is maintained as central, interacting roughly uniformly with other participating dimensions.

As noted in the paper, to efficiently compute the action of the Hamiltonian and quantum time-evolution operator on a

DOI: 10.1021/acs.jctc.8b01113
J. Chem. Theory Comput. 2019, 15, 2780−2796

wavepacket represented using tensor networks, it is required that kinetic, potential, and time-evolution operators also independently be described in the same tensor network form. See Figure 13 for a pictorial description of this process. The associated tensorial description of the potential is discussed in section V.B. The kinetic energy operator may be written in direct product form using distributed approximating functionals (DAFs)[86,87] as

$$\tilde{K}^{(2)}(x_i^{\kappa}, x_i^{\kappa'}) = \frac{1}{\sigma\sqrt{2\pi}}\left(\frac{-1}{\sigma\sqrt{2}}\right)^k \exp\left\{-\frac{(x_i^{\kappa} - x_i^{\kappa'})^2}{2\sigma^2}\right\} \sum_{n=0}^{M_{\mathrm{DAF}}/2}\left(\frac{-1}{4}\right)^n \frac{1}{n!} H_{2n+2}\left(\frac{x_i^{\kappa} - x_i^{\kappa'}}{\sqrt{2}\,\sigma}\right) \tag{B1}$$

where x_i^{κ} depicts the κth grid point along dimension x_i. The free propagator is also written using distributed approximating functionals (DAFs)[86,87] as

$$\tilde{K}(x_i^{\kappa}, x_i^{\kappa'}; \Delta t) = \frac{1}{\sigma(0)\sqrt{2\pi}} \exp\left\{-\frac{(x_i^{\kappa} - x_i^{\kappa'})^2}{2\sigma(\Delta t)^2}\right\} \times \sum_{n=0}^{M_{\mathrm{DAF}}/2}\left(\frac{\sigma(0)}{\sigma(\Delta t)}\right)^{2n+1}\left(\frac{-1}{4}\right)^n \frac{1}{n!} H_{2n}\left(\frac{x_i^{\kappa} - x_i^{\kappa'}}{\sqrt{2}\,\sigma(\Delta t)}\right) \tag{B2}$$

Here $\{\sigma(\Delta t)\}^2 = \sigma(0)^2 + \imath\Delta t\hbar/M_{QM}$, H_{2n}, and H_{2n+2} are even-order Hermite polynomials, the parameters M_{DAF} and $\sigma(0)$ above together determine the accuracy and efficiency of the DAF-propagator (eq 2) and derivative operator (eq 1).

The action of the kinetic energy operator on the wavepacket represented in tensorial form (such as eq 6) rigorously preserves this form at every step according to

$$\begin{aligned}
\nabla_{\bar{x}}^2\Phi(\bar{x}) &= \sum_{\bar{\alpha}}\left[\left(\sum_{\kappa'}\tilde{K}^{(2)}(x_1^{\kappa}, x_1^{\kappa'})\chi_{\alpha_1}^1(x_1^{\kappa'})\right) \times \left\{\Pi_{i=2}^{\mathcal{D}-1}\chi_{\alpha_{i-1},\alpha_i}^i(x_i)\right\} \times \chi_{\alpha_{\mathcal{D}-1}}^{\mathcal{D}}(x_{\mathcal{D}})\right] + \sum_{\bar{\alpha}}\left[\chi_{\alpha_1}^1(x_1) \times \left(\sum_{\kappa'}\tilde{K}^{(2)}(x_2^{\kappa}, x_2^{\kappa'})\chi_{\alpha_1,\alpha_2}^2(x_2^{\kappa'})\right)\right. \\
&\left.\left\{\Pi_{i=3}^{\mathcal{D}-1}\chi_{\alpha_{i-1},\alpha_i}^i(x_i)\right\} \times \chi_{\alpha_{\mathcal{D}-1}}^{\mathcal{D}}(x_{\mathcal{D}})\right] + \\
&\cdots = \sum_{\bar{\alpha}}\left[\chi_{\alpha_1}^{1,(2)}(x_1) \times \left\{\Pi_{i=2}^{\mathcal{D}-1}\chi_{\alpha_{i-1},\alpha_i}^i(x_i)\right\} \times \chi_{\alpha_{\mathcal{D}-1}}^{\mathcal{D}}(x_{\mathcal{D}})\right] \\
&+ \sum_{\bar{\alpha}}\left[\chi_{\alpha_1}^1(x_1) \times \chi_{\alpha_1,\alpha_2}^{2,(2)}(x_2)\left\{\Pi_{i=3}^{\mathcal{D}-1}\chi_{\alpha_{i-1},\alpha_i}^i(x_i)\right\} \times \chi_{\alpha_{\mathcal{D}-1}}^{\mathcal{D}}(x_{\mathcal{D}})\right] +
\end{aligned} \tag{B3}$$

where we have introduced in the second equation, $\chi_{\alpha_1}^{1,(2)}(x_1) \equiv (\sum_{\kappa'}\tilde{K}^{(2)}(x_1^{\kappa}, x_1^{\kappa'})\chi_{\alpha_1}^1(x_1^{\kappa'}))$, $\chi_{\alpha_1,\alpha_2}^{2,(2)}(x_2) \equiv \left(\sum_{\kappa'}\tilde{K}^{(2)}(x_2^{\kappa}, x_2^{\kappa'})\chi_{\alpha_1,\alpha_2}^2(x_2^{\kappa'})\right)$ and so on, to exemplify the MPS form of the second equation. Similarly for free-propagation

$$\begin{aligned}
\Phi(\bar{x};\, t + \Delta t) &= \sum_{\bar{\alpha}}\left[\left(\sum_{\kappa'}\tilde{K}(x_1^{\kappa}, x_1^{\kappa'};\, \Delta t)\chi_{\alpha_1}^1(x_1^{\kappa'};\, t)\right)\right. \\
&\times \left\{\Pi_{i=2}^{\mathcal{D}-1}\left(\sum_{\kappa'}\tilde{K}(x_i^{\kappa}, x_i^{\kappa'};\, \Delta t)\chi_{\alpha_{i-1},\alpha_i}^i(x_i^{\kappa'};\, t)\right)\right\} \\
&\left.\times \left(\sum_{\kappa'}\tilde{K}(x_{\mathcal{D}}^{\kappa}, x_{\mathcal{D}}^{\kappa'};\, \Delta t)\chi_{\alpha_{\mathcal{D}-1}}^{\mathcal{D}}(x_{\mathcal{D}};\, t)\right)\right] \\
&= \sum_{\bar{\alpha}}\left[\chi_{\alpha_1}^1(x_1;\, t + \Delta t) \times \left\{\Pi_{i=2}^{\mathcal{D}-1}\chi_{\alpha_{i-1},\alpha_i}^i(x_i;\, t + \Delta t)\right\}\right. \\
&\left.\times \chi_{\alpha_{\mathcal{D}-1}}^{\mathcal{D}}(x_{\mathcal{D}};\, t + \Delta t)\right]
\end{aligned} \tag{B4}$$

Furthermore, the structure $\tilde{K}(x_i^{\kappa}, x_i^{\kappa'}) \equiv \tilde{K}(|x_i^{\kappa} - x_i^{\kappa'}|)$ for both eqs 1 and B2 results in a banded Toeplitz matrix representation[86−88,98−100] for any finite M_{DAF} and $\sigma(0)$, where all diagonal elements are equal and similarly all nth super (and sub) diagonal elements are equal. This yields great advantages in storage and computation[101] for the individual operations $\chi_{\alpha_{i-1},\alpha_i}^i(x_i;\, t + \Delta t) \equiv (\sum_{\kappa'}\tilde{K}(x_i^{\kappa}, x_i^{\kappa'};\, \Delta t)\chi_{\alpha_{i-1},\alpha_i}^i(x_i^{\kappa'};\, t))$ (in eq 4) and $\chi_{\alpha_{i-1},\alpha_i}^{i,(2)}(x_i) \equiv (\sum_{\kappa'}\tilde{K}^{(2)}(x_i^{\kappa}, x_i^{\kappa'})\chi_{\alpha_{i-1},\alpha_i}^i(x_i^{\kappa'}))$ (in eq 3). As discussed in ref 102, computational efficiency for these calculations arises through reduction of these operations to a sequence of BLAS-2 "$aX + Y$" processes, where "a" is a number and "X" and "Y" are vectors.

In light of the successful tensor decomposition of the grid potential along the lines of eqs 7, 21, and 22, as highlighted by Figures 15 and 16, one may also consider the reduced complexity of the action of the potential energy operator on a wavepacket, both written in MPS form

$$\begin{aligned}
&\int \mathrm{d}\bar{x'}\delta(\bar{x} - \bar{x'})\tilde{\mathbf{V}}(\bar{x'})\Psi(\bar{x'}) = \tilde{\mathbf{V}}(\bar{x})\Psi \\
&(\bar{x}) = \sum_{\bar{\alpha},\bar{\beta}}\{\mathcal{V}_{\alpha_1}^1(x_1) \times \chi_{\beta_1}^1(x_1)\} \\
&\times \left(\Pi_{i=2}^{\mathcal{D}-1}\{\mathcal{V}_{\alpha_{i-1},\alpha_i}^i(x_i) \times \chi_{\beta_{i-1},\beta_i}^i(x_i)\}\right) \\
&\times \{\mathcal{V}_{\alpha_{\mathcal{D}-1}}^{\mathcal{D}}(x_{\mathcal{D}}) \times \chi_{\beta_{\mathcal{D}-1}}^{\mathcal{D}}(x_{\mathcal{D}})\} = \sum_{\bar{\alpha},\bar{\beta}}\chi_{\alpha_1,\beta_1}^{1,V}(x_1) \\
&\times \left(\Pi_{i=2}^{\mathcal{D}-1}\chi_{\alpha_{i-1},\alpha_i,\beta_{i-1},\beta_i}^{i,V}(x_i)\right) \times \chi_{\alpha_{\mathcal{D}-1},\beta_{\mathcal{D}-1}}^{\mathcal{D},V}(x_{\mathcal{D}})
\end{aligned} \tag{B5}$$

It clear upon inspection of this expression that there are $[\beta_1 \times \alpha_1]$ one-dimensional functions created in x_1. Similarly, there are $[\beta_i \times \alpha_i]$ one-dimensional functions created in x_i, thus presenting a potential increase in the number of such one-dimensional function. But we also note, as per eqs 5 and 7 that the singular values have been absorbed into the one-dimensional functions, and hence, we expect the contributions from the higher product singular values to progressively reduce. These aspects will be probed in future publications.

AUTHOR INFORMATION

Corresponding Author

*Email: iyengar@indiana.edu.

ORCID

Srinivasan S. Iyengar: 0000-0001-6526-2907

DOI: 10.1021/acs.jctc.8b01113
J. Chem. Theory Comput. 2019, 15, 2780−2796

Notes

The authors declare no competing financial interest.

■ ACKNOWLEDGMENTS

This research is supported by the National Science Foundation grant NSF CHE-1665336 to S.S.I. Author N.D. also gratefully acknowledges support from the Kenneth Kratz Family Charitable Foundation.

■ REFERENCES

(1) Feynman, R. P.; Hey, J.; Allen, R. W. *Feynman Lectures on Computation*; Addison-Wesley Longman Publishing Co., Inc., 1998.
(2) Nielsen, M. A.; Chuang, I. L. *Quantum computation and quantum information*; Cambridge University Press: Cambridge, 2000.
(3) Berman, L. The complexity of logical theories. *Theoretical Computer Science* **1980**, *11*, 71−77.
(4) Feynman, R. P. Simulating physics with computers. *Int. J. Theor. Phys.* **1982**, *21*, 467−488.
(5) Baesens, C.; Guckenheimer, J.; Kim, S.; MacKay, R. Three coupled oscillators: mode-locking, global bifurcations and toroidal chaos. *Phys. D* **1991**, *49*, 387−475.
(6) White, S. R. Density matrix formulation for quantum renormalization groups. *Phys. Rev. Lett.* **1992**, *69*, 2863−2866.
(7) Schollwöck, U. The density-matrix renormalization group in the age of matrix product states. *Ann. Phys.* **2011**, *326*, 96−192 January 2011 Special Issue .
(8) Schollwöck, U. The density-matrix renormalization group. *Rev. Mod. Phys.* **2005**, *77*, 259−315.
(9) Keller, S. F.; Reiher, M. Determining Factors for the Accuracy of DMRG in Chemistry. *Chimia* **2014**, *68*, 200−203.
(10) Moritz, G.; Reiher, M. Decomposition of density matrix renormalization group states into a Slater determinant basis. *J. Chem. Phys.* **2007**, *126*, 244109.
(11) Stemmle, C.; Paulus, B.; Legeza, O. Analysis of electron-correlation effects in strongly correlated systems (N_2 and N_2^+) by applying the density-matrix renormalization-group method and quantum information theory. *Phys. Rev. A: At., Mol., Opt. Phys.* **2018**, *97*, 022505.
(12) Schütt, K. T.; Arbabzadah, F.; Chmiela, S.; Müller, K. R.; Tkatchenko, A. Quantum-chemical insights from deep tensor neural networks. *Nat. Commun.* **2017**, *8*, 13890.
(13) Szalay, S.; Pfeffer, M.; Murg, V.; Barcza, G.; Verstraete, F.; Schneider, R.; Legeza, O. Tensor product methods and entanglement optimization for ab initio quantum chemistry. *Int. J. Quantum Chem.* **2015**, *115*, 1342−1391.
(14) Orús, R. A practical introduction to tensor networks: Matrix product states and projected entangled pair states. *Ann. Phys.* **2014**, *349*, 117−158.
(15) Chan, G. K.-L.; Keselman, A.; Nakatani, N.; Li, Z.; White, S. R. Matrix product operators, matrix product states, and ab initio density matrix renormalization group algorithms. *J. Chem. Phys.* **2016**, *145*, 014102.
(16) Wall, M. L.; Carr, L. D. Out-of-equilibrium dynamics with matrix product states. *New J. Phys.* **2012**, *14*, 125015.
(17) Pirvu, B.; Murg, V.; Cirac, J. I.; Verstraete, F. Matrix product operator representations. *New J. Phys.* **2010**, *12*, 025012.
(18) Gunst, K.; Verstraete, F.; Wouters, S.; Legeza, O.; Van Neck, D. T3NS: Three-Legged Tree Tensor Network States. *J. Chem. Theory Comput.* **2018**, *14*, 2026−2033.
(19) Eisert, J.; Cramer, M.; Plenio, M. B. Colloquium: Area laws for the entanglement entropy. *Rev. Mod. Phys.* **2010**, *82*, 277−306.
(20) Accardi, L. Topics in quantum probability. *Phys. Rep.* **1981**, *77*, 169−192.
(21) Ekert, A.; Knight, P. L. Entangled quantum systems and the Schmidt decomposition. *Am. J. Phys.* **1995**, *63*, 415−423.
(22) Mintert, F.; Viviescas, C.; Buchleitner, A. Basic Concepts of Entangled States. In *Entanglement and Decoherence: Foundations and Modern Trends*; Buchleitner, A., Viviescas, C., Tiersch, M., Eds.; Springer Berlin Heidelberg, 2009.
(23) Pathak, A. *Elements of quantum computation and quantum communication*; Taylor & Francis, 2013.
(24) Huang, Z.; Kais, S. Entanglement as measure of electronelectron correlation in quantum chemistry calculations. *Chem. Phys. Lett.* **2005**, *413*, 1−5.
(25) Wang, H.; Kais, S. Quantum Entanglement and Electron Correlation in Molecular Systems. *Isr. J. Chem.* **2007**, *47*, 59−65.
(26) Rajwade, A.; Rangarajan, A.; Banerjee, A. Image Denoising Using the Higher Order Singular Value Decomposition. *IEEE Transactions on Pattern Analysis and Machine Intelligence* **2013**, *35*, 849−862.
(27) Hu, C.; Lu, X.; Ye, M.; Zeng, W. Singular value decomposition and local near neighbors for face recognition under varying illumination. *Pattern Recognition* **2017**, *64*, 60−83.
(28) Iqbal, N.; Zerguine, A.; Kaka, S.; Al-Shuhail, A. Automated SVD filtering of time-frequency distribution for enhancing the SNR of microseismic/microquake events. *Journal of Geophysics and Engineering* **2016**, *13*, 964.
(29) Hassanpour, H. A timefrequency approach for noise reduction. *Digital Signal Processing* **2008**, *18*, 728−738.
(30) Martin, C. D.; Porter, M. A. The Extraordinary SVD. *American Mathematical Monthly* **2012**, *119*, 838−851.
(31) Golub, G. H.; Reinsch, C. Singular value decomposition and least squares solutions. *Numerische Mathematik* **1970**, *14*, 403−420.
(32) Martinez, M.; Harder, H.; Kubistin, D.; Rudolf, M.; Bozem, H.; Eerdekens, G.; Fischer, H.; Kluepfel, T.; Gurk, C.; Koenigstedt, R.; Parchatka, U.; Schiller, C. L.; Stickler, A.; Williams, J.; Lelieveld, J. Hydroxyl radicals in the tropical troposphere over the Suriname rainforest: air-borne measurements. *Atmos. Chem. Phys.* **2010**, *10*, 3759−3773.
(33) Peeters, J.; Nguyen, T. L.; Vereecken, L. HOx Radical Regeneration in the Oxidation of Isoprene. *Phys. Chem. Chem. Phys.* **2009**, *11*, 5935.
(34) Nguyen, T. L.; Vereecken, L.; Peeters, J. HO_x Regeneration in the Oxidation of Isoprene III: Theoretical Study of the Key Isomerisation of the Z-δ-Hydroxy-Peroxy Isoprene Radicals. *ChemPhysChem* **2010**, *11*, 3996.
(35) Peeters, J.; Muller, J.-F.; Stavrakou, T.; Nguyen, V. S. Hydroxyl Radical Recycling in Isoprene Oxidation Driven by Hydrogen Bonding and Hydrogen Tunneling: The Upgraded LIM1Mechanism. *J. Phys. Chem. A* **2014**, *118*, 8625.
(36) Sillman, S. Tropospheric Ozone: The Debate over Control Strategies. *Annu. Rev. Energy Env.* **1993**, *18*, 31.
(37) Heard, D. E.; Pilling, M. J. Measurement of OH and HO_2 in the Troposphere. *Chem. Rev.* **2003**, *103*, 5163.
(38) Tan, D.; Faloona, I.; Simpas, J. B.; Brune, W.; Shepson, P. B.; Couch, T. L.; Sumner, A. L.; Carroll, M. A.; Thornberry, T.; Apel, E.; Riemer, D.; Stockwell, W. HO_x Budgets in a Deciduous Forest: Results from the PROPHET Summer 1998 Campaign. *Journal of geophysical research-atmospheres* **2001**, *106*, 24407.
(39) Carslaw, N.; Creasey, D. J.; Harrison, D.; Heard, D. E.; Hunter, M. C.; Jacobs, P. J.; Jenkin, M. E.; Lee, J. D.; Lewis, A. C.; Pilling, M. J.; Saunders, S. M.; Seakins, P. W. OH and HO2 Radical Chemistry in a Forested Region of North-Western Greece. *Atmos. Environ.* **2001**, *35*, 4725.
(40) Guenther, A. Atmospheric Chemistry: Are Plant Emissions Green? *Nature* **2008**, *452*, 701.
(41) Lelieveld, J.; Butler, T. M.; Crowley, J. N.; Dillon, T. J.; Fischer, H.; Ganzeveld, L.; Harder, H.; Lawrence, M. G.; Martinez, M.; Taraborrelli, D.; Williams, J. Atmospheric Oxidation Capacity Sustained by a Tropical Forest. *Nature* **2008**, *452*, 737.
(42) DeGregorio, N.; Iyengar, S. S. Efficient and Adaptive Methods for Computing Accurate Potential Surfaces for Quantum Nuclear Effects: Applications to Hydrogen-Transfer Reactions. *J. Chem. Theory Comput.* **2018**, *14*, 30−47.
(43) Iyengar, S. S.; Sumner, I.; Jakowski, J. Hydrogen Tunneling in an Enzyme Active Site: A Quantum Wavepacket Dynamical Perspective. *J. Phys. Chem. B* **2008**, *112*, 7601.

DOI: 10.1021/acs.jctc.8b01113
J. Chem. Theory Comput. 2019, 15, 2780−2796

(44) Prociuk, A. H.; Iyengar, S. S. A Multi-Wavelet Treatment of the Quantum Subsystem in Quantum Wavepacket Ab-Initio Molecular Dynamics Through an Hierarchical Partitioning of Momentum Space. *J. Chem. Theory Comput.* **2014**, *10*, 2950.
(45) Leclerc, A.; Carrington, T. Calculating vibrational spectra with sum of product basis functions without storing full-dimensional vectors or matrices. *J. Chem. Phys.* **2014**, *140*, 174111.
(46) Lill, J. V.; Parker, G. A.; Light, J. C. Discrete Variable Representations and Sudden Models in Quantum Scattering-Theory. *Chem. Phys. Lett.* **1982**, *89*, 483.
(47) Light, J. C.; Hamilton, I. P.; Lill, J. V. *J. Chem. Phys.* **1985**, *82*, 1400.
(48) Hu, S.; Goldman, D. I.; Kouri, D. J.; Hoffman, D. K.; Swinney, H. L.; Gunaratne, G. H. Stages of Relaxation of Patterns and the Role of Stochasticity in the Final Stage. *Nonlinearity* **2004**, *17*, 1535.
(49) Shen, L. X.; Papadakis, M.; Kakadiaris, I. A.; Konstantinidis, I.; Kouri, D. J.; Hoffman, D. K. Image Denoising Using a Tight Frame. *IEEE transactions on image processing* **2006**, *15*, 1254.
(50) Wei, G. W.; Althorpe, S. C.; Kouri, D. J.; Hoffman, D. K. An Application of Distributed Approximating Functional-Wavelets to Reactive Scattering. *J. Chem. Phys.* **1998**, *108*, 7065.
(51) Hoffman, D. K.; Wei, G. W.; Zhang, D. S.; Kouri, D. J. Interpolating Distributed Approximating Functionals. *Phys. Rev. E: Stat. Phys., Plasmas, Fluids, Relat. Interdiscip. Top.* **1998**, *57*, 6152.
(52) Iyengar, S. S.; Parker, G. A.; Kouri, D. J.; Hoffman, D. K. Symmetry-Adapted Distributed Approximating Functionals: Theory and Application to the Ro-Vibrational States of H_3^+. *J. Chem. Phys.* **1999**, *110*, 10283.
(53) Chandler, C.; Gibson, A. Uniform Approximation of Functions with Discrete Approximation Functionals. *J. Approx. Theory* **1999**, *100*, 233.
(54) Lancaster, P.; Salkauskas, K. *Curve and Surface Fitting*; Academic, New York, 1986.
(55) De Lathauwer, L.; De Moor, B.; Vandewalle, J. A Multilinear Singular Value Decomposition. *SIAM Journal on Matrix Analysis and Applications* **2000**, *21*, 1253−1278.
(56) Tucker, L. R. The extension of factor analysis to three-dimensional matrices. In *Contributions to Mathematical Psychology*; Gulliksen, H., Frederiksen, N., Eds.; Rinehart & Winston: New York, 1964; pp 109−127.
(57) Peláez, D.; Meyer, H.-D. The multigrid POTFIT (MGPF) method: Grid representations of potentials for quantum dynamics of large systems. *J. Chem. Phys.* **2013**, *138*, 014108.
(58) García-Ripoll, J. J. Time evolution of matrix product states. *New J. Phys.* **2006**, *8*, 305.
(59) Verstraete, F.; Murg, V.; Cirac, J. Matrix product states, projected entangled pair states, and variational renormalization group methods for quantum spin systems. *Adv. Phys.* **2008**, *57*, 143−224.
(60) Greene, S. M.; Batista, V. S. Tensor-Train Split-Operator Fourier Transform (TT-SOFT) Method: Multidimensional Nonadiabatic Quantum Dynamics. *J. Chem. Theory Comput.* **2017**, *13*, 4034−4042.
(61) Baiardi, A.; Stein, C. J.; Barone, V.; Reiher, M. Vibrational Density Matrix Renormalization Group. *J. Chem. Theory Comput.* **2017**, *13*, 3764−3777.
(62) Worth, G. A.; Meyer, H.-D.; Cederbaum, L. S. Relaxation of a system with a conical intersection coupled to a bath: A benchmark 24-dimensional wave packet study treating the environment explicitly. *J. Chem. Phys.* **1998**, *109*, 3518−3529.
(63) Worth, G.; Meyer, H.-D.; Cederbaum, L. State filtering by a bath: up to 24 mode numerically exact wavepacket propagations. *Chem. Phys. Lett.* **1999**, *299*, 451−456.
(64) Raab, A.; Worth, G. A.; Meyer, H.-D.; Cederbaum, L. S. Molecular dynamics of pyrazine after excitation to the S2 electronic state using a realistic 24-mode model Hamiltonian. *J. Chem. Phys.* **1999**, *110*, 936−946.
(65) Shannon, C. A Mathematical Theory of Communication. *Bell Syst. Tech. J.* **1948**, *27*, 379.
(66) Shannon, C. Communication in the Presence of Noise. *Proc. IEEE* **1998**, *86*, 447.
(67) Press, W. H.; Teukolsky, S. A.; Vetterling, W. T.; Flannery, B. P. *Numerical Recipes in C*; Cambridge University Press: New York, 1992.
(68) Jäckle, A.; Meyer, H. Product representation of potential energy surfaces. *J. Chem. Phys.* **1996**, *104*, 7974−7984.
(69) Manzhos, S.; Carrington, T. Using neural networks to represent potential surfaces as sums of products. *J. Chem. Phys.* **2006**, *125*, 194105.
(70) Avila, G.; Carrington, T. Using a pruned basis, a non-product quadrature grid, and the exact Watson normal-coordinate kinetic energy operator to solve the vibrational Schrdinger equation for C2H4. *J. Chem. Phys.* **2011**, *135*, 064101.
(71) Avila, G.; Carrington, T. Using nonproduct quadrature grids to solve the vibrational Schrdinger equation in 12D. *J. Chem. Phys.* **2011**, *134*, 054126.
(72) Meyer, H.-D.; Manthe, U.; Cederbaum, L. S. The Multi-Configurational Time-Dependent Hartree Approach. *Chem. Phys. Lett.* **1990**, *165*, 73.
(73) Wang, H.; Thoss, M. Multilayer formulation of the multi-configuration time-dependent Hartree theory. *J. Chem. Phys.* **2003**, *119*, 1289−1299.
(74) Beck, M. H.; Jackle, A.; Worth, G. A.; Meyer, H.-D. *Phys. Rep.* **2000**, *324*, 1.
(75) Otto, F. Multi-layer Potfit: An accurate potential representation for efficient high-dimensional quantum dynamics. *J. Chem. Phys.* **2014**, *140*, 014106.
(76) Chan, G. K.-L.; Head-Gordon, M. Highly correlated calculations with a polynomial cost algorithm: A study of the density matrix renormalization group. *J. Chem. Phys.* **2002**, *116*, 4462−4476.
(77) Marti, K. H.; Ondik, I. M.; Moritz, G.; Reiher, M. Density matrix renormalization group calculations on relative energies of transition metal complexes and clusters. *J. Chem. Phys.* **2008**, *128*, 014104.
(78) Kurashige, Y.; Yanai, T. High-performance ab initio density matrix renormalization group method: Applicability to large-scale multireference problems for metal compounds. *J. Chem. Phys.* **2009**, *130*, 234114.
(79) Mizukami, W.; Kurashige, Y.; Yanai, T. More π Electrons Make a Difference: Emergence of Many Radicals on Graphene Nanoribbons Studied by Ab Initio DMRG Theory. *J. Chem. Theory Comput.* **2013**, *9*, 401−407.
(80) Schuch, N.; Wolf, M. M.; Verstraete, F.; Cirac, J. I. Computational Complexity of Projected Entangled Pair States. *Phys. Rev. Lett.* **2007**, *98*, 140506.
(81) Oseledets, I. Tensor-Train Decomposition. *SIAM Journal on Scientific Computing* **2011**, *33*, 2295−2317.
(82) Teng, A. P.; Crounse, J. D.; Wennberg, P. O. Isoprene Peroxy Radical Dynamics. *J. Am. Chem. Soc.* **2017**, *139*, 5367−5377.
(83) Sumner, I.; Iyengar, S. S. Analysis of Hydrogen Tunneling in an Enzyme Active Site Using Von Neumann Measurements. *J. Chem. Theory Comput.* **2010**, *6*, 1698.
(84) Verstraete, F.; Cirac, J. I. Matrix product states represent ground states faithfully. *Phys. Rev. B: Condens. Matter Mater. Phys.* **2006**, *73*, 094423.
(85) Osborne, T. J.; Nielsen, M. A. Entanglement in a simple quantum phase transition. *Phys. Rev. A: At., Mol., Opt. Phys.* **2002**, *66*, 032110.
(86) Kouri, D. J.; Huang, Y.; Hoffman, D. K. Iterated Real-Time Path Integral Evaluation Using a Distributed Approximating Functional Propagator and Average-Case Complexity Integration. *Phys. Rev. Lett.* **1995**, *75*, 49.
(87) Hoffman, D. K.; Nayar, N.; Sharafeddin, O. A.; Kouri, D. J. Analytic Banded Approximation for the Discretized Free Propagator. *J. Phys. Chem.* **1991**, *95*, 8299.
(88) Iyengar, S. S. *Ab Initio* Dynamics with Wave-Packets and Density Matrices. *Theor. Chem. Acc.* **2006**, *116*, 326.
(89) Bowman, J. M.; Carrington, T.; Meyer, H.-D. Variational quantum approaches for computing vibrational energies of polyatomic molecules. *Mol. Phys.* **2008**, *106*, 2145−2182.
(90) Baranov, V.; Oseledets, I. Fitting high-dimensional potential energy surface using active subspace and tensor train (AS+TT) method. *J. Chem. Phys.* **2015**, *143*, 174107.

DOI: 10.1021/acs.jctc.8b01113
J. Chem. Theory Comput. 2019, 15, 2780−2796

(91) Brommer, P.; Gahler, F. Potfit: effective potentials from ab initio data. *Modell. Simul. Mater. Sci. Eng.* **2007**, *15*, 295.
(92) Brommer, P.; Kiselev, A.; Schopf, D.; Beck, P.; Roth, J.; Trebin, H.-R. Classical interaction potentials for diverse materials from ab initio data: a review of potfit. *Modell. Simul. Mater. Sci. Eng.* **2015**, *23*, 074002.
(93) Jakowski, J.; Sumner, I.; Iyengar, S. S. Computational Improvements to Quantum Wavepacket Ab Initio Molecular Dynamics Using a Potential-Adapted, Time-Dependent Deterministic Sampling Technique. *J. Chem. Theory Comput.* **2006**, *2*, 1203.
(94) Sumner, I.; Iyengar, S. S. Quantum Wavepacket *Ab Initio* Molecular Dynamics: An Approach for Computing Dynamically Averaged Vibrational Spectra Including Critical Nuclear Quantum Effects. *J. Phys. Chem. A* **2007**, *111*, 10313.
(95) Hocker, D.; Li, X.; Iyengar, S. S. Shannon Information Entropy Based Time-Dependent Deterministic Sampling Techniques for Efficient "on-The-Fly" Quantum Dynamics and Electronic Structure. *J. Chem. Theory Comput.* **2011**, *7*, 256.
(96) Li, R. On Multi-Mesh *H*-Adaptive Methods. *J. Sci. Comput.* **2005**, *24*, 321.
(97) Bartels, R. H.; Beatty, J. C.; Barsky, B. A. *An Introduction to Splines for Use in Computer Graphics and Geometric Modeling*; Morgan Kaufman Publishers, Inc., Los Altos, CA, 1987.
(98) Korevaar, J. Pansions and the Theory of Fourier Transforms. *Am. Math. Soc. Trans.* **1959**, *91*, 53.
(99) Yu, S.; Zhao, S.; Wei, G. W. Local Spectral Time Splitting Method for First- and Second-Order Partial Differential Equations. *J. Comput. Phys.* **2005**, *206*, 727.
(100) Iyengar, S. S.; Jakowski, J. Quantum Wavepacket Ab Initio Molecular Dynamics: An Approach to Study Quantum Dynamics in Large Systems. *J. Chem. Phys.* **2005**, *122*, 114105.
(101) Pacheco, A. B.; Iyengar, S. S. A Multi-Stage *Ab-Initio* Quantum Wavepacket Dynamics Formalism for Electronic Structure and Dynamics in Open Systems. *J. Chem. Phys.* **2010**, *133*, 044105.
(102) Pacheco, A. B.; Iyengar, S. S. Multi-Stage *Ab-Initio* Quantum Wavepacket Dynamics for Electronic Structure and Dynamics in Open Systems: Momentum Representation, Coupled Electron Nuclear Dynamics and External Fields. *J. Chem. Phys.* **2011**, *134*, 074107.

DOI: 10.1021/acs.jctc.8b01113
J. Chem. Theory Comput. 2019, 15, 2780−2796